NASA TECHNICAL NOTE

NASA TN D-6333

NASA TN D-6333

ANALYTICAL AND EXPERIMENTAL STUDY OF COMPRESSIBLE LAMINAR-FLOW HEAT TRANSFER AND PRESSURE DROP OF A GAS IN A UNIFORMLY HEATED TUBE

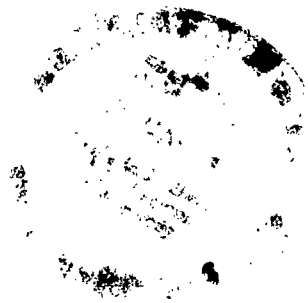

by Alden F. Presler

Lewis Research Center
Cleveland, Ohio 44135

NATIONAL AERONAUTICS AND SPACE ADMINISTRATION • WASHINGTON, D. C. • APRIL 1971

1. Report No. NASA TN D-6333	2. Government Accession No.	3. Recipient's Catalog No.
4. Title and Subtitle ANALYTICAL AND EXPERIMENTAL STUDY OF COMPRESSIBLE LAMINAR-FLOW HEAT TRANSFER AND PRESSURE DROP OF A GAS IN A UNIFORMLY HEATED TUBE		5. Report Date April 1971 6. Performing Organization Code
7. Author(s) Alden F. Presler		8. Performing Organization Report No. E-5702 10. Work Unit No. 127-01
9. Performing Organization Name and Address Lewis Research Center National Aeronautics and Space Administration Cleveland, Ohio 44135		11. Contract or Grant No. 13. Type of Report and Period Covered Technical Note
12. Sponsoring Agency Name and Address National Aeronautics and Space Administration Washington, D.C. 20546		14. Sponsoring Agency Code

15. Supplementary Notes

16. Abstract

Numerical solutions of the compressible laminar boundary-layer equations are obtained to investigate acceleration effects due to wall heating on axial development of velocity and temperature profiles, local Nusselt numbers, and especially static pressure drop and its momentum and frictional components. Heating, combined with compressibility, produces blunter velocity and temperature profiles than are reported in earlier analyses. Larger momentum pressure drops relative to friction losses reduce the Poiseuille pressure parameter by as much as one-third of its fully developed value. Experimental values of pressure drop and momentum-to-friction pressure ratio checks the analytical preductions.

17. Key Words (Suggested by Author(s)) Pressure drop; Gas flow; Pressure distribution; RT pressure drop; Heat transfer; Forced convection; Temperature profiles; Laminar flow	18. Distribution Statement Unclassified - unlimited		
19. Security Classif. (of this report) Unclassified	20. Security Classif. (of this page) Unclassified	21. No. of Pages 45	22. Price* $3.00

*For sale by the National Technical Information Service, Springfield, Virginia 22151

ANALYTICAL AND EXPERIMENTAL STUDY OF COMPRESSIBLE LAMINAR-FLOW HEAT TRANSFER AND PRESSURE DROP OF A GAS IN A UNIFORMLY HEATED TUBE

by Alden F. Presler

Lewis Research Center

SUMMARY

This is the report of an analytical and an experimental investigation to determine what effect acceleration caused by heat input to a compressible gas has on the laminar Nusselt numbers and static pressure drops. Helium gas flow in a circular tube was studied with uniform entrance conditions and wall heat flux conditions.

The analytical portion considers the compressible laminar momentum and energy boundary-layer equations to be valid throughout the tube cross section and axially downstream from the entrance. A numerical finite difference marching technique is used to solve the equations and is adaptable to a wide range of values of physical parameters such as heat flux and entrance Mach number. Axial development of velocity and temperature profiles, Nusselt numbers, and static pressures were calculated for a 200-fold range in heat flux. Local bulk Nusselt numbers are little affected by thermal acceleration, but pressure drops from flow acceleration by heating show large increases due to heat flux.

The experiment closely approximates the geometrical and physical model of the analysis. There is a fivefold variation of the experimental heat flux, and entrance Mach numbers vary from 0.035 to 0.10. Experimentally determined Nusselt numbers and overall static pressure drops confirm analytical results, which were obtained for corresponding heat flux parameters and dimensionless tube lengths.

INTRODUCTION

This report is a continuation of two previous numerical studies of the effect of heat flux level on the behavior of the laminar flow of a compressible gas in a uniformly heated circular tube for both heating and cooling. Reference 1 reported the heat-

transfer and frictional behavior of both adiabatic laminar flow and one diabatic laminar case for a helium gas model. Reference 2 examined in detail by numerical analysis the flow behavior of helium gas undergoing cooling. It was found in both these reports that certain important deviations from classical heat-transfer and frictional results occurred because of compressibility effects at low subsonic Mach numbers.

The present report examines in more detail analytically and experimentally the heating effect on local Nusselt numbers and frictional and pressure parameters. In the analytical program a 200-fold variation of heat flux level is imposed on the uniform entrance flow. In particular the development of momentum and frictional pressure components in the flow is detailed for this range of heat fluxes.

An experiment is described in which heat-transfer measurements are made on the laminar flow of helium gas in an electrically heated small-diameter Inconel tube. Local Nusselt numbers, inlet-to-exit pressure drop, and pressure drop components due to momentum change and friction loss are determined for a range of wall- to bulk-temperature ratios of 1.4 to 1.7. These experimental results are compared with numerical predictions from the analytical model.

Reference 3 was one of the earliest analyses of laminar flow heat transfer that considered temperature variation of the physical properties. This analysis assumed fully developed velocity profiles in the circular tube. Constant property analyses for heat transfer to laminar incompressible flow for developing profiles are given in references 4 and 5.

Laminar flow heat-transfer experiments have not been numerous. A uniform heat flux program with both up and down flow in a vertical tube is reported in reference 6. The object of that research was to establish criteria for when free-convection effects are important relative to the forced convection. An experiment similar to the one reported herein is described in reference 7. It contains local Nusselt numbers for both helium and nitrogen flows and friction factors based on wall shear stresses, but it has no data on flow pressure drops.

Correlation of laminar friction and heat-transfer data of reference 7 is given in reference 8. The experimental friction factor based on wall shear stress is normalized to the fully developed analytical value by a product transformation of the ratio of wall to bulk temperature.

A recent numerical analysis using the marching technique is reported in reference 9. The condition of uniform heat flux was applied to a laminar flow which had initially a fully developed velocity profile. Besides the Nusselt number development, only friction factors based on wall shear stress were shown.

SYMBOLS

Variables and dimensional quantities:

a	local sound velocity, $\sqrt{\gamma Rt}$
C_p	specific heat at constant pressure
C_V	specific heat at constant volume
D	tube diameter
G	mass velocity, $\dot{W}/\pi r_W^2$
h	heat-transfer coefficient, $q_W/(t_W - t_b)$
k	thermal conductivity
L	length of test section
p	absolute static pressure
$\dot{Q}$	rate of energy dissipation
q_w	wall heat flux
r	radius
t	absolute static temperature
u	axial velocity component
v	radial velocity component
$\dot{W}$	flow rate, mass per unit time
z	axial distance from entrance
μ	viscosity
ρ	density
τ	shear stress
$\bar{\tau}$	average shear stress over axial distance z

Dimensionless quantities:

C_p'	specific heat ratio $C_p/C_{p,e}$
$f_{p,b}$	friction factor based on pressure drop from inlet, with density and velocity evaluated at local bulk temperature, $\left(\frac{1}{2}\right)(p_e - p)\Big/\left(\frac{z}{D}\right)\rho_b u_b^2$
$f_{\tau,b}$	local friction factor based on wall shear stress, with density and velocity evaluated at local bulk temperature, $2\tau_w/\rho_b u_b^2$

Gz	Graetz number, $\left[(Re)(Pr)_e\right]/(z/D)$
K	thermal conductivity ratio, k/k_e
M	local Mach number, u/a
Nu_b	bulk Nusselt number, hD/k_b
P	pressure drop from inlet, $(p_e - p)/\rho_e u_e^2$
Pr	Prandtl number, $C_p\mu/k$
Q^+	wall heat flux, $q_w r_w/k_e t_e$
R	radius ratio, r/r_w
Re	Reynolds number, GD/μ
T	static temperature, $(1 - t/t_e)/Q^+$
U	axial velocity component, u/u_e
V	radial velocity component, $2Re_e(v/u_e)$
Z	axial distance, $(z/D)/Re$
Z^+	axial distance, $(z/D)/Re_b$
γ	specific heat ratio, C_p/C_v
ϵ	total emissivity
θ	temperature ratio, $(t - t_w)/(t_b - t_w)$
μ'	viscosity, μ/μ_e
ρ'	density, ρ/ρ_e
τ_w'	shear stress at wall, $\tau_w r_w/\mu_e\mu_e$

Subscripts:

b	bulk conditions
℄	tube centerline conditions
d	downstream mixing box conditions
e	entry (initial) conditions
FR	friction
i	inside tube wall conditions
j	node point in axial position
k	node point in radial position

M momentum

o outside tube wall conditions

w wall conditions

NUMERICAL ANALYSIS

The steady-state compressible momentum and energy boundary-layer equations and the compressible continuity equation, in axisymmetric cylindrical coordinates, were transformed in reference 2 to the following nondimensional system:

$$\rho'\left(U\frac{\partial U}{\partial Z}+V\frac{\partial U}{\partial R}\right)=\frac{dP}{dZ}+\frac{4}{R}\frac{\partial}{\partial R}\left(\mu' R\frac{\partial U}{\partial R}\right) \tag{1}$$

$$\rho' C_p'\left(U\frac{\partial T}{\partial Z}+V\frac{\partial T}{\partial R}\right)-\frac{(\gamma-1)M_e^2}{Q^+}U\frac{dP}{dZ}=\frac{4}{Pr_e}\frac{1}{R}\frac{\partial}{\partial R}\left(KR\frac{\partial T}{\partial R}\right)-\frac{4(\gamma-1)M_e^2}{Q^+}\mu'\left(\frac{\partial U}{\partial R}\right)^2 \tag{2}$$

$$\frac{\partial \rho' U}{\partial Z}+\frac{1}{R}\frac{\partial}{\partial R}(\rho' VR)=0 \tag{3}$$

The dependent variables are the axial and radial velocities U and V, the static temperature T, and static pressure P. The independent variables are the radial and axial distances R and Z. And the physical properties are density ρ', specific heat C_p', isentropic coefficient γ, viscosity μ', and thermal conductivity K. The system parameters are Prandtl number at the entrance Pr_e, entrance Mach number M_e, and uniform wall heat flux Q^+.

The transformations reflect the conditions of uniform heat flux, and uniform initial flow at the entrance to the tube, as shown in figure 1.

The transformed perfect gas law is

$$\rho' = \frac{1-\gamma M_e^2 P}{1-Q^+ T} \tag{4}$$

The appropriate boundary conditions are

Initial ($Z = 0,\ 0 \le R \le 1$):

$$\left.\begin{aligned} U &= 1 \\ V &= 0 \\ P &= 0 \\ T &= 0 \end{aligned}\right\} \tag{5}$$

Centerline ($Z > 0$, $R = 0$):

$$\left.\begin{aligned} V &= 0 \\ \frac{\partial U}{\partial R} &= \frac{\partial T}{\partial R} = 0 \end{aligned}\right\} \tag{6}$$

Wall ($Z > 0$, $R = 1$):

$$\left.\begin{aligned} U &= V = 0 \\ \frac{\partial T}{\partial R} &= -\frac{1}{K(Z,1)} \end{aligned}\right\} \tag{7}$$

Thermal and transport properties appropriate to helium gas (ref. 1) are evaluated by the special relations

$$\left.\begin{aligned} \mu' = K = \left(\frac{t}{t_e}\right)^{0.68} &= (1 - Q^+T)^{0.68} \\ C_p' &= 1 \\ Pr_e &= \frac{2}{3} \\ \gamma &= \frac{5}{3} \end{aligned}\right\} \tag{8}$$

The numerical solution of the system described above by the marching technique (see appendix) for given Q^+ and M_e, provides values of $U(R,Z)$, $T(R,Z)$, and $P(Z)$ as numerical output. Also included as output are the bulk velocity and temperature, $U_b(Z)$ and $T_b(Z)$, respectively. From these, the heat-transfer parameter

$$Nu_b = \frac{2}{K_b(T_w - T_b)} \tag{9}$$

is immediately calculated, where from equation (8)

$$K_b = \mu_b' = \left(1 - Q^+ T_b\right)^{0.68} \tag{10}$$

(ref. 1).

The two friction parameters of interest in this study are obtained from the numerical data. The first, based on local wall shear, is

$$4f_{\tau,b}Re_b = \frac{16\tau_w'}{\mu_b' U_b} \tag{11}$$

where

$$\tau_w' = \frac{\tau_w r_w}{\mu_e u_e} \tag{12}$$

The second, based on the overall pressure change, is

$$4f_{pb}Re_b = \frac{2P}{U_b Z^+} \tag{13}$$

where $Z^+ = (z/D)/Re_b$ is a dimensionless distance based on bulk Reynolds number.

The overall static pressure drop is the sum of the drop due to friction and the drop due to momentum change,

$$\Delta p = \Delta p_{friction} + \Delta p_{momentum} \tag{14}$$

Divide these terms by $\rho_e u_e^2$,

$$\frac{\Delta p}{\rho_e u_e^2} = \frac{\Delta p_{FR}}{\rho_e u_e^2} + \frac{\Delta p_M}{\rho_e u_e^2} \tag{15}$$

The left side of equation (15) is the dimensionless pressure P. Then the equation can be written as

$$P = P_{FR} + P_M \tag{16}$$

where the dimensionless pressure terms on the right have the form (ref. 2)

$$P_{FR} = \frac{4\bar{\tau}_w}{\rho_e u_e^2}\left(\frac{Z}{D}\right) \tag{17}$$

and

$$P_M = U_b - 1 \tag{18}$$

The wall shear stress in equation (17) is an average over the length Z.

The bulk velocities calculated in the numerical program are used in equation (18) to calculate the dimensionless momentum pressure drop occurring between the entrance and the local axial position. As the overall static pressure P is also calculated as a function of axial position, the dimensionless friction pressure P_{FR} is immediately calculated from equation (16) for the required local axial positions.

The relative distribution of the friction and momentum pressure drop contributions is immediately given by the ratio P_M/P_{FR}.

EXPERIMENTAL INVESTIGATION

The heat-transfer and pressure drop rig, shown schematically in figure 2, consists essentially of an electrically heated tube mounted vertically in a vacuum chamber.

The vacuum chamber is a vertically mounted steel cylinder, 4 feet (1.2 m) high and 18 inches (0.46 m) in diameter. The interior was sandblasted to reduce outgassing time. Access to the tank is through an opening 12 inches (0.30 m) wide and about

4 feet (1.2 m) long. A flange has an O-ring seal which holds the working vacuum to around 5 microns pressure. The test section is mounted on the inside of the door, which is hinged on the bottom, so that when the door is open the test section is outside the vacuum chamber and is therefore easily accessible.

Flow Measurements

Helium gas from the six-tank manifold is metered through a parallel bank of four rotameters (see fig. 2). Gas pressure at the flowmeters is controlled at 30 psig (101 000 N/m^2). Primary flow control is by means of valves downstream of the rotameters. Further control is by means of a valve on the exit side of the test section.

The four rotameters were calibrated with helium gas at 45 psia and 80° F. They have maximum flow rates of 0.00030, 0.0027, 0.011, and 0.027 pound per minute (1.1×10^{-8}, 1×10^{-7}, 3.7×10^{-7} and 1×10^{-6} kg/sec). This gives a maximum flow rate with all four tubes at capacity of 0.041 pound per minute (1.54×10^{-6} kg/sec).

Test Section

The test section is constructed of Inconel alloy 600 tubing whose outside diameter is 0.125 inch (0.308 cm) and inside diameter is 0.089 inch (0.226 cm). Briefly, the test section 19 inches (48.2 cm) long between the heating electrodes and 23 inches (58.4 cm) long between the static pressure taps.

The general dimensions of the instrumented test section are given in figure 3. The plenum chambers for static pressure measurements and the wall thermocouples, are discussed in the next two instrumentation sections.

Inconel was chosen because of its fine high temperature strength properties and because its electrical resistance varies but slightly over a wide range of temperatures (ref. 10). Inconel alloy 600 has a liquidus temperature of 2600° F (1692 K) and a solidus temperature of 2540° F (1669 K) (ref. 11). The physical properties of Inconel alloy 600 needed for the present study are found in references 10 to 12, and are reproduced in figure 4 for the applicable temperature range.

Pressure Measurements

The static pressure drop of the gas flowing through the heated test section was obtained from the two tap positions at the entrance and exit of the tube, shown in figures

2 and 3. Each tap position consists of a cylindrical plenum chamber of 3/4-inch (1.91-cm) diameter Inconel alloy 600 tubing 3/4-inch (1.91-cm) long and welded to the flow tube, with the chamber fed through four 4-mil holes drilled along crossed diameters. The inside of holes were carefully deburred after drilling. Details of the plenum are shown in figure 3.

Pressure leads of 1/8-inch (0.318-cm) Inconel tubing are connected to the plenum chambers by threaded fittings, and the pressure leads are brought through the vacuum chamber bulkhead with nylon fittings. Outside the vacuum chamber, plastic tubing connects the two pressure leads to a U-tube manometer, 4 feet (1.2 m) long, which can be positioned at 0°, 30°, 45°, and 60° from the vertical. The manometer is half filled with acetylene tetrabromide colored with a red dye. This fluid has a specific gravity of 2.967 ($20^{\circ}/4^{\circ}$), has a formula weight of 345.70, and is safe to use (ref. 13 formula e-265, pg. C-308). It serves well as manometer fluid for uses between water, on one hand, and mercury, on the other.

A second U-tube manometer half filled with mercury is attached in parallel with the tetrabromide manometer for cases when pressure drops are too large for the first manometer. In this case, shutoff valves on the tetrabromide manometer seal it from the system.

Temperature Measurements

Wall temperatures on the test section are obtained from nineteen 24-gage chromel-alumel thermocouples, which were spot welded at the positions indicated on figure 3. These thermocouples are positioned alternately 180° around the tube, and are spaced closer together at both the exit and entrance sections where the temperature gradients are steeper. The thermocouple wires are encased in ceramic beads for insulation and thermal shielding.

Figure 3 indicates a pair of thermocouples spot welded 3 inches apart on both the downstream and upstream pressure tap tubing. These thermocouples, installed to measure thermal gradients on the plenum tubine for heat loss calculations, are also encased in ceramic beads.

The two copper bus bars connecting the power to the Inconel test section within the vacuum enclosure also have a pair of chromel-alumel thermocouples spotted on them for the same purpose of measuring the thermal gradients. On the upstream bus, the couples are placed 8 inches (20.3 cm) apart, while on the downstream bus the couples are 12 inches (30.48 cm) apart.

Upstream and downstream mixing box temperatures are measured with Inconel sheathed chromel-alumel thermocouple probes inserted at right angles to the gas flow

in the mixing cans. A sheathed thermocouple probe is similarly placed in the plenum chamber of the rotameters in order to measure the flow temperatures for correcting the indicated flow.

All thermocouple leads are brought through the vacuum tank bulkhead in sealed couplings and then to switching boxes outside the tank. Temperatures were recorded on flight recorder charts and monitored on a self-balancing potentiometer. The mixing box temperature difference is also checked with a precision laboratory potentiometer.

Voltage and Current Measurements

The current fed to the test section is measured with a precision milliammeter connected to a current transformer with a step-down ratio of 240:1. Voltages at the six taps were measured with calibrated laboratory voltmeters.

DATA REDUCTION

The experimental program provides the following output:

(1) Test section wall temperatures
(2) Mixing box probe temperatures
(3) Temperature gradients on the bus bars and the two plenum leads
(4) Mass flow rate of helium through the test section
(5) Electrical current in the test section
(6) Voltage drops across the test section and the graphite electrodes
(7) Pressure at the entrance to the test section and total pressure drop across the working section

The first concern in data reduction is that of overall heat balance. For this the total energy input rate is the sum of the wattage in the test section and the wattage in the graphite electrodes.

$$\dot{Q}_{\text{total input}} = \dot{Q}_{\text{test section}} + \dot{Q}_{\text{electrodes}} \tag{19}$$

These wattages are obtained from the measured current and voltages of the appropriate taps.

Energy losses to the environment are the radiation flux from the heated test section and the conduction losses in the bus bars, in the plenum leads, and out the two ends of the test section.

$$\dot{Q}_{loss,\,total} = \dot{Q}_{rad} + \dot{Q}_{bus} + \dot{Q}_{plenum} + \dot{Q}_{tube\ end} \tag{20}$$

The heat balance then equates the net heat input with the temperature rise between the mixing boxes.

$$\dot{Q}_{net} = \dot{Q}_{total\ input} - \dot{Q}_{total\ losses} \equiv \dot{W}C_p(t_d - t_e) \tag{21}$$

The losses consist of all heat not used to raise the gas temperature, as indicated in equation (20). The preceding equality, of course, is rarely achieved in a heat-transfer experiment because of the uncertainties in the laboratory meters. However, this calculation must be performed as a check to give confidence in the calculation of the local net heat flux used in later heat-transfer correlations.

In the heat loss calculations, the conduction terms $\dot{Q}_{bus}$, $\dot{Q}_{plenum}$, and $\dot{Q}_{tube\ end}$ are calculated from

$$\dot{Q}_{cond} = -kA\frac{\Delta t}{\Delta L} \tag{22}$$

where the thermal conductivity k is appropriate to the metal under consideration, A is the cross sectional area normal to the direction of heat flux, and $\Delta t/\Delta L$ is the temperature gradient obtained from the pair of thermocouples spaced L units apart (for the plenum and bus bars) or the gradient obtained from the test section wall temperatures. For the present experiment, conduction along the Inconel tubing (i.e., the test section and plenum leads) is no more than 1 percent of the total losses. This is due to the low thermal conductivity of Inconel (fig. 4(a)) and the very small cross section of the tubing.

Heat loss due to radiation from the test section to the inner wall is essentially radiation between concentric cylinders, infinitely long, of which the area of the outer cylinder (vacuum tank) is essentially infinite in value compared with the radiating surface of the small inner cylinder (test section). For this extreme but appropriate case, the net radiation exchange for diffuse radiation is given by (ref. 14, pg. 4, eq. (31-9))

$$q_{rad} = \epsilon\sigma\left(t_{tube}^4 - t_{enclosure}^4\right) \tag{23}$$

where the flux is based on unit area of the outer surface of the tube, the temperatures are absolute, σ is the Stefan-Boltzmann constant, and ϵ is the emissivity factor of the

heated test section. Since the tube temperature varies along the length from inlet to outlet, the total radiation heat loss is the integral

$$\dot{Q}_{\text{total rad}} = 2\pi r_o \int_0^L q_{\text{rad}}\, dx \tag{24}$$

along the tube length. We know the tube temperature, however, only at 19 positions on the heated portion (fig. 3). We therefore replace the integral by the summation over n incremental areas

$$\dot{Q}_{\text{total rad}} = \sum_j \dot{Q}_{\text{rad},j} (j = 1, \ldots, 19) \tag{25}$$

where

$$\left.\begin{aligned} \dot{Q}_{\text{rad},j} &= q_{\text{rad},j}\, \Delta A_j \\ &= q_{\text{rad},j} \cdot 2\pi r_o\, \Delta L_j \end{aligned}\right\} \tag{26}$$

Here

$$q_{\text{rad},j} = \sigma\epsilon\left(t_j^4 - t_{\text{enclosure}}^4\right) \tag{27}$$

where the enclosure temperature was at 311 K (560° R), and t_j is the absolute tube temperature at the j^{th} thermocouple. The incremental area $\Delta A_j (= 2\pi r_o\, \Delta L_j)$ is taken so that the thermocouple is at the midpoint of the small length ΔL_j.

The emissivity of a heated tube is a complicated function of temperature, surface conditions (smoothness, degree of oxidation) and previous metals history such as annealing. Data on emissivity of Inconel alloy 600 is collected in reference 12 and is reproduced in figure 4(c). The experimental runs reported herein were conducted at wall temperatures less than 867 K (1100° F), and thus the solid lower curve in figure 4(c) seems appropriate to this calculation. However, an emissivity value of 0.4 is chosen to represent the tube for these data at all tube positions. The choice of this value was arrived at from trial heat balances starting with emissivity values 0.2. The higher value of 0.4 gave good balances for all experimental runs. It appears that the aging process, which produces the almost constant and larger emissivities shown in fig-

ure 4(c), also affected our test section in its many hours of heating at temperatures of 800 K and lower. This is probably the physical reason underlying the constant (and empirically determined) emissivity of 0.4.

The practical equation for radiation loss to be used for the present data reduction is

$$\dot{Q}_{\text{total rad}} = 2\pi r_o \sigma\epsilon\left(\sum_j t_j^4 \, \Delta L_j - t_{\text{encl}}^4 \sum_j \Delta L_j\right) = 2\pi r_o \sigma\epsilon \sum_j t_j^4 \, \Delta L_j - 2\pi r_o \sigma\epsilon L t_{\text{encl}}^4 \tag{28}$$

where $r_o = 0.125$ inch (0.315 cm); L = 19 inches (48.3 cm); $t_{\text{encl}} = 560^{\circ}$ R (311 K); $\epsilon = 0.4$; and $\sigma = 5.73\times10^{-12}$ watts per square centimeter per K^4.

The total radiation loss calculated by the preceding technique, along with the conduction losses from the bus bars, are the total losses $\dot{Q}_{\text{loss}}$ used in computing the net heat input of equation (21).

The local net heat flux needed for computing the local Nusselt numbers are obtained from

$$q_{\text{net},j} \, \Delta A_{\text{inner},j} = \left(Q_{\text{input},j}\right)''' \pi\left(r_o^2 - r_i^2\right)\Delta L_j - q_{\text{rad},j} \, \Delta L_{\text{outer},j} \tag{29}$$

for the incremental areas $\Delta A_{\text{inner},j}(= \pi r_i \, \Delta L_j)$ and $\Delta A_{\text{outer},j}(= \pi r_o \, \Delta L_j)$ containing the j^{th} thermocouple. Here the first term on the right hand side of equation (20) is the electrical energy dissipated in the tube in the volume contained in the length ΔL_j. Thus

$$q_{\text{net},j} = \left(Q_{\text{input},j}\right)'''\left(\frac{r_o^2 - r_i^2}{r_i}\right) - q_{\text{rad},j}\left(\frac{r_o}{r_i}\right) \tag{30}$$

is the expression used to directly compute the heat flux need in the Nusselt number.

The temperature drop across the thin tube wall is calculated by equation (2.14-d) of reference 15. The most severe drop occurs when the outer surface is perfectly insulated. In this special case, and for the heat input rates of the present work, the maximum temperature drop across the tube wall is in the order of 1 K, which is negligible for this study. Consequently, the wall temperature used in the heat transfer calculations are the indicated recorder temperatures.

The local bulk Nusselt numbers may now be computed at each of the j thermocouple positions using the net heat flux from equation (30):

$$Nu_{b\,j} = \frac{2r_i q_{net,j}}{\left[k_b(t_w - t_b)\right]_j} \tag{31}$$

At each thermocouple position j, the local bulk Reynolds number is, from its definition,

$$Re_{b\,j} = \frac{2\dot{W}}{\pi r_i (\mu_b)_j} \tag{32}$$

In equations (31) and (32) the values of the helium thermal conductivity k_b and viscosity μ_b are determined at the local bulk temperature t_b from the transport property data of reference 16, which is also plotted in figure 5.

RESULTS AND DISCUSSION

Analytical

The system of equations and boundary conditions (1) to (8) are solved numerically by a marching technique (see appendix) for radial variations of U and T, and for axial variations in U, T, and P. From the solutions the Nusselt numbers and friction factors, equations (9), (11) and (13), are obtained as a function of position along the tube. Calculations are carried out for values of initial Mach number of 0.0005, 0.004, and 0.06, and of the heat flux parameter $Q^+ = 0.135$, 1.35, 13.5 and 27.0. Numerical results of axial velocity profiles for several axial positions, initial Mach numbers, and heat flux parameters, are shown in figure 6.

Hornbeck (ref. 17) shows the velocity profile development from initial uniform conditions for constant property fluids to the fully developed parabolic (Poiseuille) profile at values of $Z^+ \sim 0.1$. This orderly profile development becomes distorted for flows of compressible fluids (variable density) with heat-induced acceleration. In the entrance regions of the tube this distortion is observed in large fluid acceleration near the wall, resulting at higher heat inputs in velocity "overshoot," that is, velocities near the wall exceeding the centerline velocity. Comparison of figures 6(a) to (d) shows that the acceleration overshoot distortion changes from an unobservable contribution at the low $Q^+ = 0.135$ to a large contribution around $Z^+ \sim 0.01$ for the high $Q^+ = 27.0$.

The overshoot distortion is smoothed out in the downstream sections of the tube; but the effects of near-wall acceleration remain, which prohibit a true fully developed flow (parabolic profile) from being obtained (figs. 6(c) to (d)).

The resulting bluntness of the downstream velocity profile, caused by heat-induced acceleration, is exactly opposite the predicted heat-transfer effect on the velocity profiles as cited in references 3 and 15 (fig. 9.16). The pioneer work of reference 3 assumed a fully developed flow; this condition eliminated transverse velocity V and axial velocity gradient $\partial U/\partial Z$ from the momentum equation to be solved. Thus the heat transfer affected the flow only through the temperature variation of the fluid viscosity and thermal conductivity. For gases this implies a profile that is blunter than parabolic for cooling, and a profile that is more peaked ($u_{\ell}/u_b > 2.0$) than parabolic for heating. The actual profiles are shown in figure 6(e) for the two cases $Q^+ = 1.35$ and $Q^+ = -1.35$. The cooling data are from reference 2.

There is a Mach number effect which intrudes only in figure 6(c) and which also has a decided flattening effect on the velocity profiles as the local bulk Mach numbers exceed 0.5 and the flow proceeds to choking. For nearly the same Z^+ the profile at local Mach number of 0.67 is much blunter than the profile at Mach number 0.39. Flow changes are occurring very rapidly in this region. No further results for this interresting effect are available because of limitations in the computational programs at the higher subsonic Mach numbers.

Heating rate effect on velocities near the wall is shown in another way in figure 7, where the centerline- to bulk-velocity ratio development with axial distance is plotted with Q^+ as parameter. Isothermal analyses for flow developing from an initial slug profile (refs. 1, 18, and 19) are plotted for comparison. The limit of u_{ℓ}/u_b of 2.0 represents fully developed Poiseuille laminar flow. There is but little deviation from the isothermal curve for the low $Q^+ = 0.135$ case. For $Q^+ = 1.35$, profile development follows isothermal up to $Z^+ \cong 0.01$ where the velocity overshoot in the wall region begins to reduce the quantity of flow in the center region of the tube, resulting in the reduced u_{ℓ}/u_b and the longer approach to Poiseuille limit. There is much greater deviation for $Q^+ = 13.5$ and 27.0, and overshoot effect begins much sooner, at around $Z^+ \cong 0.001$. At the highest heating rates, there is a minimum ratio around $Z^+ \cong 0.03$. This means that, while the bulk and centerline velocity both increase under heating, relatively more flow is carried in the wall overshoot region than in the center portion of the tube in the region $0.001 < Z^+ < 0.005$.

The decrease in the u_{ℓ}/u_b ratio for $Q^+ = 13.5$ and $M_e = 0.06$ in the region of $Z^+ > 0.10$ is due, as mentioned earlier, to the flattening of the profile in the upper subsonic Mach number regime.

The inclusion of variable density and inertia-convective terms in the numerical boundary-layer heat-transfer analysis has yielded the unusual acceleration effects on axial velocity development which are shown in figures 6 and 7. Temperature profiles suffer a similar distortion from the same causes.

The intensity of acceleration effects on both $T(Z,R)$ and $U(Z,R)$ is directly related to the heat flux level Q^+, and this result is apparent for the dimensionless temperatures in figure 8 where there is a progressive 200-fold increase in the wall heat flux. The following qualitative discussion of the acceleration effect on the variable θ is applicable to gas flows at all heat flux levels, but it is most graphically illustrated at the highest flux in figure 8(d).

In the entrance portion of the tube, the accelerating gas in the wall region convects most of the heat flux from the wall; the central bulk of the flow remains at constant temperature up to axial lengths of about $Gz^{-1} \sim 0.01$.

Downstream of this Gz^{-1} position, heat flux penetrates to the centerline of the tube. However, the continuing heat-induced acceleration of the gas flow finally produces temperature profiles in the usually fully developed tube regions that are blunter than the classical results of reference 3. The profiles in the latter work were calculated using realistic gas transport properties, but without the disturbing effect of axial velocity gradients which are associated with the radial convection that mixes the central bulk of the flow.

The result from reference 3 which is plotted on figure 8(d) for purpose of comparison is at the value of $t_w/t_b = 1.7$; this corresponds to $Gz^{-1} = 0.07$ in the present case of $Q^+ = 27.0$.

The deviation of the present results from reference 3 is rather opposite to that classical prediction in that the downstream blunt profiles in figure 8 are similar to the cooling heat transfer cases of the earlier work. There, with the absence of radial convection, cold gas at the wall sustained a large radial temperature gradient (due to low thermal conductivity), but the interior flow showed a rather blunt temperature profile, that is, with shallow curvature, because of the higher thermal conductivity of the warmer gas.

In figure 8(c), for $Q^+ = 13.5$, the additional effect of high subsonic Mach number becomes apparent in the difference in the curves for the same $Gz^{-1} = 0.37$ but with different initial Mach numbers. The solid curve for $Gz^{-1} = 0.37$ has a local bulk Mach number of about 0.67, the same as the velocity curve in figure 6(d).

Since wall-to-bulk temperature ratios have been used as parameters in correlating high temperature heat transfer data (ref. 8) it is interesting to observe the variation of that ratio with axial distance. Figure 9 details the development in ascending values of the heat parameter Q^+. In all cases, the wall temperatures are close to the bulk temperatures in the immediate region of the tube entrance, which is due to mixing from the very high convection where the wall velocity gradients are very steep, and also to conduction caused by steep local temperature gradients. Farther down the tube, the developing velocities give rise to substantial wall-to-bulk temperature differences and, hence, increasing temperature ratios. With the approach to a fully developed condition

the wall-to-bulk temperature difference becomes almost a constant. However, the simultaneous and approximately equal rise in wall and bulk temperature implies that the ratio of absolute temperatures approaches a value of unity as a limit.

All the numerical cases in figure 9 show a maximum in t_w/t_b, the value of which increases with increasing Q^+. The position of the maximum on the G_z^{-1} axis decreases with increasing values of the heat parameter Q^+. This inverse relation between Q^+ and axial position of maximum temperature ratio simply reflects the influence of the more rapid rise of t_w and t_b, and the larger $t_w - t_b$ difference at higher wall heat fluxes.

Numerical results for the Nusselt number in developing flow are shown in figure 10. These cases are all for low values of initial Mach number, so there is no choking or near choking effects in these data. The most interesting result of these calculations is the insensitivity of the fully developed Nusselt number to the level of wall heat flux. Even for values of $Q^+ = 13.5$ and 27.0, the Nusselt numbers approach the classical uniform heat flux $Nu_b = 48/11$ as $Gz^{-1} \to \infty$ (ref. 15, p. 239). This result contrasts sharply with the cooling heat-transfer behavior of helium in reference 2, where the fully developed Nusselt number was about 75 percent higher than classical uniform heat flux value.

The laminar friction parameters of equations (11) and (13) are shown in figures 11 and 12, respectively, as development with axial distance. The shear friction parameter in figure 11 is strongly influenced in the entrance region by the level of the heat flux parameter Q^+. This is a result of the fluid velocity overshoot near the wall, as in indicated in figure 7. The steep velocity gradients in the entrance wall region naturally give rise to large wall shear.

The low Q^+ cases and the adiabatic results from reference 1 approach the fully developed Poiseuille value of $4f_{\tau,b}Re_b = 64$. The higher Q^+ cases could approach a slightly higher asymptotic value of, perhaps 68. Because of excessive computer time needed, these calculations were not carried out quite far enough to definitely establish such a value.

Both the $Q^+ = 13.5$ and 27.0 cases give identical friction parameter values for $Z^+ > 0.10$ when the initial Mach numbers are very low. For a $M_e = 0.06$, however, the $Q^+ = 13.5$ case exhibits a choking effect when $Z > 0.2$. This result was first reported in reference 1 and is due to the steepening of the velocity profile near the wall for the high subsonic flows. This profile development is shown in figure 6(d).

The friction parameter $4f_{p,b}Re_b$, based on the pressure drop from the tube entrance to the local Z^+ position, is shown in figure 12 for the four Q^+ values. The low Q^+ cases approach the fully developed Poiseuille limit of $4f_{p,b}Re_b = 64$. The higher Q^+ cases seem to approach an asymptote of 40, but its more precise value is also not established because the calculations were not carried out for larger Z^+ because of the

excessive computer time required. The pressure drop friction parameter for $Q^+ = 13.5$ and $M_e = 0.06$ dips sharply for values of $Z^+ > 0.2$ which, again, is the region of high subsonic Mach number effect.

The dimensionless pressure drop P used to calculate $4f_{p,b}Re_b$ in the previous figure, is shown in figure 13 as a development with axial distance Z^+ and with Q^+ as parameter. For the higher heating case $Q^+ = 13.5$, the friction pressure drop P_{FR} is also detailed. This was calculated from equations (16) and (18) in the manner described in the theory section of this report. Two cases for $Q^+ = 13.5$ are shown, with $M_e = 0.0005$ and 0.06. For $M_e = 0.06$, the choking effect is again seen at the upper Z^+ limits of the calculation. Figure 13 is useful for obtaining the theoretical P values needed for comparison with experimental pressure drop data.

The relative distribution of momentum and friction pressure drops, shown in figure 14 as P_M/P_{FR} against Z^+, is a sensitive indicator of the changes in the velocity profiles along the tube axis. This is most true at the higher heat fluxed $Q^+ = 13.5$ and 27.0. The very steep velocity gradients at tube entrance, as noted previously, produce high wall shear stress which overwhelms in magnitude the P_M from the small rise in bulk velocity in that region.

Experimental

Experimental and analytical results for heat transfer and shear friction are compared in figures 15 and 16, respectively. In figure 15, experimental local Nusselt numbers from the present study, and also helium data from reference 7, are plotted along with the numerical adiabatic line for developing uniform heat flux case. The first 10 percent of the tube length are more sensitive to thermocouple errors because the wall- to bulk-temperature differences are small, especially relative to the fully developed values. Scatter in experimental data is much less pronounced in the downstream tube sections, which is demonstrated by the maximum ±25 percent deviation of the data around the asymptotic value $Nu_b = 48/11$ for large Z^+ (ref. 1). Such deviation is acceptable in laminar heat-transfer experiments (ref. 7), and we therefore conclude that measurement and data reduction of variables such as mass flow, temperatures, and net heat flux, are correct.

No local wall shear values were obtained in the present experiment. However, Davenport (ref. 7) reported local friction factors for his heat-transfer experiments with helium gas. His values, based on local bulk conditions, are plotted on figure 16, and they are compared with analytical results for adiabatic case ($Q^+ = 0$) and for one high heat flux case ($Q^+ = 13.5$) both of which also appear in figure 11. The experimental friction parameters have the most scatter in the entrance region ($Z^+ < 0.04$ for most

runs). This is where determination of the axial pressure gradient (needed for calculation of the local wall shear stress from pressure tap data) is most inaccurate. In the downstream regions of the tube, the experimental friction parameters seem to converge in the limit to the analytical prediction.

Table I gives the pressure drop results for eight experimental runs. Comparison is made in the last two columns with analytical predictions corresponding to the same Z^+ value as the experimental. Since the analytical results in figure 13 for P_T and in figure 14 for P_M/P_{FR} are at values of $Q^+ = 0.135$, 1.35, 13.5, and 27.0, these last

TABLE I. - COMPARISON OF EXPERIMENTAL AND NUMERICAL PRESSURE DROP BEHAVIOR

Experimental								Numerical	
Entrance Mach number, M_e	Exit Mach number, M_o	Entrance Reynolds number, Re_e	Wall heat flux, Q^+	Pressure drop from inlet, P	Momentum-to friction-pressure ratio, P_M/P_{FR}	Axial distance, N^+	Pressure drop parameter, $4f_{p,b}Re_b$	Pressure drop from inlet, P	Momentum-to friction-pressure ratio, P_M/P_{FR}
0.0348	0.0434	1890	0.35	9.97	0.061	0.186	68.0	9.0	0.080
.0441	.0792	2450	1.65	21.8	.102	.180	61.9	20.0	.130
.0459	.0742	2440	1.00	14.1	.107	.196	60.6	13.5	.135
.0460	.0781	2440	1.29	19.6	.100	.216	64.7	19.0	.130
.0471	.0774	2410	1.13	16.4	.105	.206	62.4	14.5	.132
.0557	.0808	2850	1.02	11.35	.097	.143	79.3	10.0	.140
.0622	.0878	2880	1.15	9.85	.098	.127	81.5	8.5	.142
.110	.201	2840	1.05	12.2	.140	.150	65.0	10.5	.140

two columns in table I are interpolated from figures 13 and 14 using the experimental Q^+ recorded in the fourth column. Agreement between the experimental and analytical values of P is quite good, about 10 percent difference in most cases.

The momentum-to-friction pressure ratio P_M/P_{FR} is more sensitive to experimental accuracy than is P. Calculation of P_M from equation (18) requires accuracy in both P and T_b at the test section exit Z^+ to give a reliable U_b. Because P_{FR} is obtained from P and P_M with equation (16), any error in P_M is reflected in P_{FR} in the opposite direction and is magnified in the ratio P_M/P_{FR}. These facts are observed in comparing the experimentally determined ratios with the analytical-numerical P_M/P_{FR} in the last column of table I. The agreement is not as good as with the static pressures P.

The experimental and analytical investigations complement each other, with the analysis guiding the experiment and the results of the analysis ultimately testing the former. Thus, it is concluded from comparison of the results of the two investigations

that the numerical marching solution of the compressible boundary-layer equations for flow in tubes gives realistic development of heat-transfer and pressure functions for the subsonic region.

The experimental runs recorded in table I are for constant heat flux, to a first approximation. The second run in the table ($M_e = 0.0441$, $Q^+ = 1.65$) does have a 16-percent decrease in flux level along the tube because of radiation loss from the higher wall temperatures, as calculated by equation (30). This results in a Q^+ change from 1.80 to 1.52. The $Q^+ = 1.65$ in the table I is the averaged heat balance value. This run was chosen, because of its more pronounced heat flux variation, to test the effects of a flux variation in the numerical program. These results will be compared with those using (1) the average constant flux from the heat balance and (2) the initial flux which would hold for the entire tube in the absence of radiation loss.

Table II contains three data columns, the first reproducing the experimental results

TABLE II. - RESULTS OF EXPERIMENTAL - ANALYTICAL COMPARISON OF PRESSURE RESULTS FOR VARIABLE HEAT FLUX

CASE $Q^+ = 1.80 - 1.52$

	Experimental	Numerical	
Q^+	1.65 (Average)	1.80 (Constant)	1.80 - 1.52 (Variable)
Re_e	2450	2450	2450
Z^+	0.180	0.180	0.180
M_e	0.0441	0.0441	0.0441
$M\ (Z^+ = 0.180)$	0.0792	0.083	0.083
P	21.8	16.8	20.0
U_b	2.97	3.18	3.20
$4f_{pb}Re_b$	61.9	58.0	64.0
P_M/P_{FR}	0.102	0.128	0.119

of the second row in table I, and the last two columns reporting the results of the fixed $Q^+ = 1.80$ and the variable Q^+ calculations. For these flux levels and flux variation, there is very little difference in pressure results from the numerical program. The agreement with the experiment for this particular run is about the same as using the heat balance average $Q^+ = 1.65$. At $Z^+ = 0.180$ the analyses for $Q^+ = 1.65$, 1.80, and 1.80 to 1.52 all gave the same value of Nu_b ($Nu_b = 4.34$).

CONCLUSIONS

The laminar, compressible, viscous flow in a uniformly heated tube was investigated both by numerical analysis and experiment. The flow of the gas entered the tube with uniform velocity and temperature and at low subsonic Mach numbers. The results may be summarized as follows:

Analytical

1. For any level of uniform wall heat flux, the local bulk Nusselt numbers exhibit only small deviations from the constant property analyses. This is in contrast to the results for the same initial conditions but with moderate wall cooling for which the nominal fully developed Nusselt numbers are about 75 percent higher than the constant property analysis value.

2. Flow acceleration due to heating causes static pressure drops to increase as the wall heat flux level is raised. However, the pressure parameter, which is formed from the pressure drop, is much less sensitive to heating levels, and in the nominally fully developed tube section is about 2/3 of the Poiseuille limit of 64.0 at the highest heat flux of the present program.

3. Velocity profiles in the fully developed tube section are somewhat blunter than Poiseuille profiles because of continued flow acceleration in the region near the heated wall. This result is contrary to the sharp profile found in heat-transfer texts where profile variations are due only to viscosity decrease from the wall temperature rise.

4. The overshoot velocity effect near the heated wall in the tube entrance does produce large shear stress in this region and contributes to larger local friction factors and pressure drops in the entrance than are obtained in constant property or adiabatic compressible analyses.

5. The static pressure development down the tube is split into the sum of the momentum and total friction pressure drops. The contribution of momentum change relative to pressure drop due to friction is larger for the higher wall heat fluxes.

Experimental

1. Experimental bulk Nusselt numbers for a fivefold variation in wall heat flux verify the analytical prediction of insensitivity of the Nusselt numbers to the heating level.

2. Static pressure drops from the experimental tests are compared with analytical values for the same dimensionless heat flux, and results from the two methods agree to within 10 percent.

3. The general conformity of the analytical and experimental pressure relation at the heat flux levels reported herein are considered as ample justification of the reliability of results and method for the numerical marching technique analysis of developing laminar compressible tube flows with heat transfer.

4. An experimental run in which the wall heat flux decreases because of radiation losses by 16 percent from inlet to exit is compared with numerical calculations with the same heat flux distribution. The numerical analysis produces values of the pressure parameters P, momentum- to friction-pressure ratio P_M/P_{FR}, and pressure drop parameter $4f_{p,b}Re_b$ which are close to the experimentally determined values of these three parameters.

Lewis Research Center,
National Aeronautics and Space Administration,
Cleveland, Ohio, January 22, 1971,
127-01.

APPENDIX - NUMERICAL PROCEDURE FOR FINITE DIFFERENCE SOLUTION OF LAMINAR FLOW BOUNDARY LAYER EQUATIONS

The nondimensionalized momentum, energy, continuity, and state equations (1) to (4) are, respectively,

$$\rho' U\left(\frac{\partial U}{\partial Z} + V \frac{\partial U}{\partial R}\right) = \frac{dP}{dZ} + \frac{4}{R} \frac{\partial}{\partial R}\left(\mu' R \frac{\partial U}{\partial R}\right) \tag{A1}$$

$$\rho' C_p'\left(U \frac{\partial T}{\partial Z} + V \frac{\partial T}{\partial R}\right) - \left[\frac{(\gamma - 1)M_e^2}{Q^+}\right] U \frac{dP}{dZ} = \frac{4}{Pr} \frac{1}{R} \frac{\partial}{\partial R}\left(RK \frac{\partial T}{\partial R}\right) - 4\left[\frac{(\gamma - 1)M_e^2}{Q^+}\right] \mu'\left(\frac{\partial U}{\partial R}\right)^2 \tag{A2}$$

$$\frac{\partial \rho' U}{\partial Z} + \frac{1}{R} \frac{\partial}{\partial R}(\rho' V R) = 0 \tag{A3}$$

$$\rho' = \frac{1 - \gamma M_e^2 P}{1 - Q^+ T} \tag{A4}$$

The finite difference analogs of equations (A1) and (A2) are obtained by replacing the derivatives in these equations by

$$\frac{\partial U}{\partial Z} \cong \frac{U_{j+1,k} - U_{j,k}}{\Delta Z} \tag{A5}$$

$$\frac{\partial U}{\partial R} \cong \frac{U_{j,k+1} - U_{j,k-1}}{2\,\Delta R} \tag{A6}$$

$$\frac{\partial^2 U}{\partial R^2} \cong \frac{U_{j,k+1} - 2U_{j,k} + U_{j,k-1}}{(\Delta R)^2} \tag{A7}$$

The mesh grid used for these differences forms are shown in figure 17. It should be noted that equations (A5) and (A7) are written in explicit form. With the coefficients evaluated at the (j,k) mesh point, the numerical scheme to be solved is

$$\rho'_{j,k}U_{j,k}\left(\frac{U_{j+1,k} - U_{j,k}}{\Delta Z}\right) = \left(\frac{dP}{dZ}\right)_j - \rho'_{j,k}V_{j,k}\left(\frac{U_{j,k+1} - U_{j,k-1}}{2\,\Delta R}\right)$$

$$+ \frac{4}{R_k}\left[\mu'_{j,k}R_k\left(\frac{U_{j,k+1} - 2U_{j,k} + U_{j,k-1}}{(\Delta R)^2}\right)\right.$$

$$\left. + \left(\frac{U_{j,k+1} - U_{j,k-1}}{2\,\Delta R}\right)\left(\mu'_{j,k} + R_k\,\frac{\mu_{j,k+1} - \mu_{j,k-1}}{2\,\Delta R}\right)\right] \qquad \text{(A8)}$$

$$\rho'_{j,k}C'_{p_{j,k}}U_{j,k}\left(\frac{T_{j+1,k} - T_{j,k}}{\Delta Z}\right) = \left[\frac{(\gamma - 1)M_e^2}{Q^+}\right]U_{j,k}\left(\frac{dP}{dZ}\right)_j - \rho'_{j,k}C'_{p_{j,k}}V_{j,k}\left(\frac{T_{j,k+1} - T_{j,k-1}}{2\,\Delta R}\right)$$

$$+ \frac{4}{Pr}\,\frac{1}{R_k}\left[K_{j,k}R_k\left(\frac{T_{j,k+1} - 2T_{j,k} + T_{j,k-1}}{(\Delta R)^2}\right)\right.$$

$$\left. + \left(\frac{T_{j,k+1} - T_{j,k-1}}{2\,\Delta R}\right)\left(K_{j,k} + R_k\,\frac{K_{j,k+1} - K_{j,k-1}}{2\,\Delta R}\right)\right]$$

$$-4\left[\frac{(\gamma - 1)M_e^2}{Q^+}\right]\mu'_{j,k}\left(\frac{U_{j,k+1} - U_{j,k-1}}{2\,\Delta R}\right)^2 \qquad \text{(A9)}$$

Equations (A8) and (A9) are used to calculate the dependent variables U and T stepwise at the mesh point (j + 1, k) from the variables and their derivatives along the radius at the preceding j^{th} axial position.

The transverse velocity $V_{j,k}$ is calculated from the continuity equation (A3) as the integral relation

$$\rho'_{j,k}V_{j,k} = \frac{1}{R_k}\int_0^{R_k} R\left(\frac{\partial \rho' U}{\partial Z}\right)dR \qquad \text{(A10)}$$

where the integral can be obtained by any appropriate quadrature method. In this work the Simpson integration formula is used.

The integrand in equation (A10) is expanded using the dimensionless equation of state (A4):

$$\rho'_{j,k}V_{j,k} = \frac{1}{R_k}\int_0^{R_k} R\left[\rho' \frac{\partial U}{\partial Z} + \frac{U}{1 - Q^+T}\left(\rho' Q^+ \frac{\partial T}{\partial Z} - \gamma M_e^2 \frac{dP}{dZ}\right)\right]_j dR \qquad \text{(A11)}$$

The derivatives on the left hand side of equations (A8) and (A9) are now expressed as

$$\frac{U_{j+1,k} - U_{j,k}}{\Delta Z} = \left(\frac{1}{\rho' U}\frac{dP}{dZ}\right)_{j,k} - \left(\frac{U_{j,k+1} - U_{j,k-1}}{2\,\Delta R}\right)\left(\frac{1}{U_{j,k}R_k}\right)\int_0^{R_k} R\left[\rho' \frac{\partial U}{\partial Z}\right.$$

$$\left. + \frac{4}{1 - Q^+T}\left(\rho' Q^+ \frac{\partial T}{\partial Z} - \gamma M_e^2 \frac{dP}{dZ}\right)\right]_j dR + \frac{4}{U_{j,k}}\left(\frac{\mu'_{j,k}}{\rho'_{j,k}}\right)\left[\frac{U_{j,k+1} - 2U_{j,k} + U_{j,k-1}}{(\Delta R)^2}\right.$$

$$\left. + \left(\frac{U_{j,k+1} - U_{j,k-1}}{2\,\Delta R}\right)\left(\frac{1}{R_k} + \frac{\mu'_{j,k+1} - \mu'_{j,k-1}}{2\mu'_{j,k}\,\Delta R}\right)\right] \qquad \text{(A12)}$$

$$\frac{T_{j+1,k} - T_{j,k}}{\Delta Z} = \left[\frac{(\gamma - 1)M_e^2}{Q^+}\right]\frac{1}{\rho'_{j,k}}\left(\frac{dP}{dZ}\right)_j - \left(\frac{T_{j,k+1} - T_{j,k-1}}{2\,\Delta R}\right)\frac{1}{U_{j,k}R_k}\int_0^{R_k} R\left[\rho' \frac{\partial U}{\partial Z}\right.$$

$$\left. + \frac{U}{1 - Q^+T}\left(\rho' Q^+ \frac{\partial T}{\partial Z} - \gamma M_e^2 \frac{dP}{dZ}\right)\right]_j dR + \frac{4}{\mathrm{Pr}\,U_{j,k}}\left(\frac{K_{j,k}}{\rho'_{j,k}}\right)\left[\frac{T_{j,k+1} - 2T_{j,k} + T_{j,k-1}}{(\Delta R)^2}\right.$$

$$\left. + \left(\frac{T_{j,k+1} - T_{j,k-1}}{2\,\Delta R}\right)\left(\frac{1}{R_k} + \frac{K_{j,k+1} - K_{j,k-1}}{2K_{j,k}\,\Delta R}\right)\right]$$

$$- 4\left[\frac{(\gamma - 1)M_e^2}{Q^+}\right]\frac{\mu'_{j,k}}{\rho'_{j,k}}\frac{1}{U_{j,k}}\left(\frac{U_{j,k+1} - U_{j,k-1}}{2\,\Delta R}\right)^2 \qquad \text{(A13)}$$

At the mesh position (j + 1,k) the expressions (A12) and (A13) make use of backward differences in U and T on the left hand side. The right hand sides make use of previous values of these variables, along with their axial and transvers derivatives, at position (j,k).

After the momentum and energy difference equations are solved for U_{j+1} and T_{j+1} at axial position (j + 1), the pressure gradient at (j + 1) is obtained from the momentum equation at the wall (R = 1) by

$$\left(\frac{dP}{dZ}\right)_{j+1} = -\left[\frac{4}{R}\frac{\partial}{\partial R}\left(\mu' R \frac{\partial U}{\partial R}\right)\right]_{\substack{R=1 \\ j+1}}$$

$$= -4\left[\mu' \frac{\partial^2 U}{\partial R^2} + \left(\mu' + \frac{\partial \mu'}{\partial R}\right)\frac{\partial U}{\partial R}\right]_{\substack{R=1 \\ j+1}} \qquad \text{(A14)}$$

The new value of dP/dZ at the (j+1) axial position is then inserted into the right hand sides of equations (A12) and (A13) for the subsequent calculations of $U_{k,j+2}$ and $T_{k,j+2}$ for k = 0 to N. The value of P_{j+1} is then obtained from the backward difference approximation

$$\left(\frac{dP}{dZ}\right)_{j+1} \cong \frac{\Delta P}{\Delta Z} = \frac{P_{j+1} - P_j}{\Delta Z} \qquad \text{(A15)}$$

The central difference approximations for the transverse derivatives used within the interior mesh points are not sufficiently accurate at the wall (k = N) because the k = N + 1 value of U and T are fictitious values within the solid boundary. Consequently, a different differencing approximation is used for the wall derivatives which uses the boundary values and several interior mesh points. This wall difference scheme is derived from a Taylor series expansion using backward differences from the wall. Thus, for any axial j position,

$$U_{N-1} = U_N - \Delta R\left(\frac{\partial U}{\partial R}\right)_N + \frac{1}{2!}(\Delta R)^2\left(\frac{\partial^2 U}{\partial R^2}\right)_N - \frac{1}{3!}(\Delta R)^3\left(\frac{\partial^3 U}{\partial R^3}\right)_N + \frac{1}{4!}(\Delta R)^4\left(\frac{\partial^4 U}{\partial R^4}\right)_N + \ldots \qquad \text{(A16)}$$

$$U_{N-2} = U_N - 2\,\Delta R\left(\frac{\partial U}{\partial R}\right)_N + \frac{4(\Delta R)^2}{2!}\left(\frac{\partial^2 U}{\partial R^2}\right)_N - \frac{8(\Delta R)^3}{3!}\left(\frac{\partial^3 U}{\partial R^3}\right)_N + \frac{16(\Delta R)^4}{4!}\left(\frac{\partial^4 U}{\partial R^4}\right)_N + \ldots \tag{A17}$$

The N, N - 1, and N - 2 subscripts in (A16) and (A17) refer to the k index. The j index has been suppressed for convenience in the derivation of the special wall derivatives, but it will reappear in the final expression for the pressure gradient where the wall derivatives are needed.

Eliminating the second derivative $(\partial^2 U/\partial R^2)_N$ between equations (A16) and (A17) gives the first derivative as

$$\left(\frac{\partial U}{\partial R}\right)_N = \frac{U_{N-2} - 4U_{N-1}}{2\,\Delta R} + \frac{1}{3}(\Delta R)^2\left(\frac{\partial^3 U}{\partial R^3}\right)_N + \ldots \tag{A18}$$

or

$$\left(\frac{\partial U}{\partial R}\right)_N \cong \frac{U_{N-2} - 4U_{N-1}}{2\,\Delta R} \tag{A19}$$

which is accurate to the order of $(\Delta R)^2$.

Eliminating the first derivatives $(\partial U/\partial R)_N$ from (A16) and (A17) gives the second derivative at the wall as

$$\left(\frac{\partial^2 U}{\partial R^2}\right)_N = \frac{U_{N-2} - 2U_{N-1}}{(\Delta R)^2} + \Delta R\left(\frac{\partial^3 U}{\partial R^3}\right)_N + \ldots \tag{A20}$$

or

$$\left(\frac{\partial^2 U}{\partial R^2}\right)_N \cong \frac{U_{N-2} - 2U_{N-1}}{(\Delta R)^2} \tag{A21}$$

which is of the order ΔR.

By substituting equations (A19) and (A21) into equation (A14), the difference form of the pressure gradient equation becomes

$$\left(\frac{dP}{dZ}\right)_{j+1} = -4\left[\mu'_{j+1,N}\,\frac{U_{j+1,N-2} - 2U_{j+1,N-1}}{(\Delta R)^2} + \left(\mu'_{j+1,N} + \frac{\mu'_{j+1,N-2} - 4\mu'_{j+1,N-1}}{2\,\Delta R}\right)\left(\frac{U_{j+1,N-2} - 4U_{j+1,N-1}}{2\,\Delta R}\right)\right] \quad \text{(A22)}$$

REFERENCES

1. Deissler, Robert G.; and Presler, Alden F.: Analysis of Developing Laminar Flow and Heat Transfer in a Tube for a Gas with Variable Properties. Proceedings of the Third International Heat Transfer Conference. Vol. 1. AIChE, 1966, pp. 250-256.

2. Presler, A. F.: Analysis of Developing Laminar Flow and Heat Transfer in a Tube for a Gas with Cooling. NASA TN D-6152, 1970.

3. Deissler, Robert G.: Analytical Investigation of Fully Developed Laminar Flow in Tubes with Heat Transfer with Fluid Properties Variable Along the Radius. NACA TN 2410, 1951.

4. Siegel, R.; Sparrow, E. M.; and Hallman, T. M.: Steady Laminar Heat Transfer in a Circular Tube with Prescribed Wall Heat Flux. Appl. Sci. Res., sec. A, vol. 7, no. 5, 1958, pp. 386-392.

5. Kays, W. M.: Numerical Solutions for Laminar-Flow Heat Transfer in Circular Tubes. Trans. ASME, vol. 77, no. 8, Nov. 1955, pp. 1265-1274.

6. Hallman, Theodore M.: Experimental Study of Combined Forced and Free Laminar Convection in a Vertical Tube. NASA TN D-1104, 1961.

7. Davenport, Monty E.: The Effect of Transverse Temperature Gradients on the Heat Transfer and Friction for Laminar Flow of Gases. Rep. TR 247-3, Stanford Univ., July 31, 1962.

8. Taylor, Maynard F.: A Method of Correlating Local and Average Friction Coefficients for Both Laminar and Turbulent Flow of Gases Through a Smooth Tube with Surface to Fluid Bulk Temperature Ratios from 0.35 to 7.35. Int. J. Heat Mass Transfer, vol. 10, no. 8, Aug. 1967, pp. 1123-1128.

9. Worsoe-Schmidt, P. M.: Heat Transfer in the Thermal Entrance Region of Circular Tubes and Annular Passages with Fully Developed Laminar Flow. Int. J. Heat Mass Transfer, vol. 10, no. 4, Apr. 1967, pp. 541-551.

10. Manly, W. D.; and Bridges, W. H.: Nickel and Its Alloys. Materials. Vol. 1 of Reactor Handbook. Second ed., C. R. Tipton, Jr., ed., Interscience Publ., Inc., 1960, ch. 27.

11. Lyman, Taylor, ed.: Metals Handbook. Vol. I. Eighth ed., American Society of Metals, 1961.

12. Wolf, J.; and Brown, W. F., Jr., eds.: Non-Ferrous Alloys. Vol. IIA of Aerospace Structural Metals Handbook, Supplement 1. Belfour Stulen, Inc. (AFML-TR-68-115), Mar. 1968.

13. Weast, Robert C., ed.: Handbook of Chemistry and Physics, 47th ed., Chemical Rubber Co., 1966.

14. Jakob, Max: Heat Transfer. Vol. II. John Wiley & Sons, Inc., 1957.

15. McAdams, William H.: Heat Transmission. Third ed., McGraw-Hill Brook Co., Inc., 1954.

16. Hornbeck, Robert W.: Laminar Flow in the Entrance Region of a Pipe. Appl. Sci. Res., Sec. A, vol. 13, 1964, pp. 224-232.

17. Langhaar, Henry L.: Steady Flow in the Transition Length of a Straight Tube. J. Appl. Mech., vol. 9, no. 2, June 1942, pp. 55-58.

18. Sparrow, E. M.; Lin, S. H.; and Lundgren, T. S.: Flow Development in the Hydrodynamic Entrance Region of Tubes and Ducts. Phys. Fluids, vol. 7, no. 3, Mar. 1964, pp. 338-347.

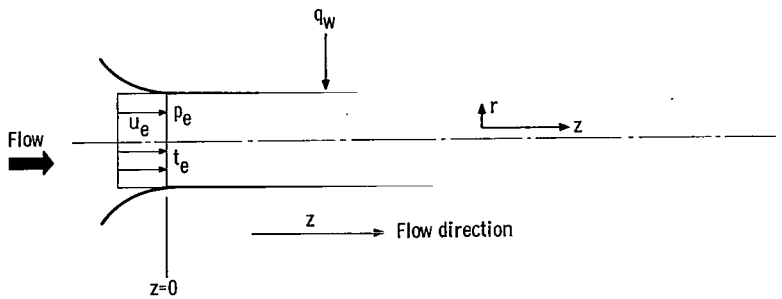

Figure 1. - Model for numerical analysis of uniform heat flux to laminar compressible flow in tube with uniform initial conditions.

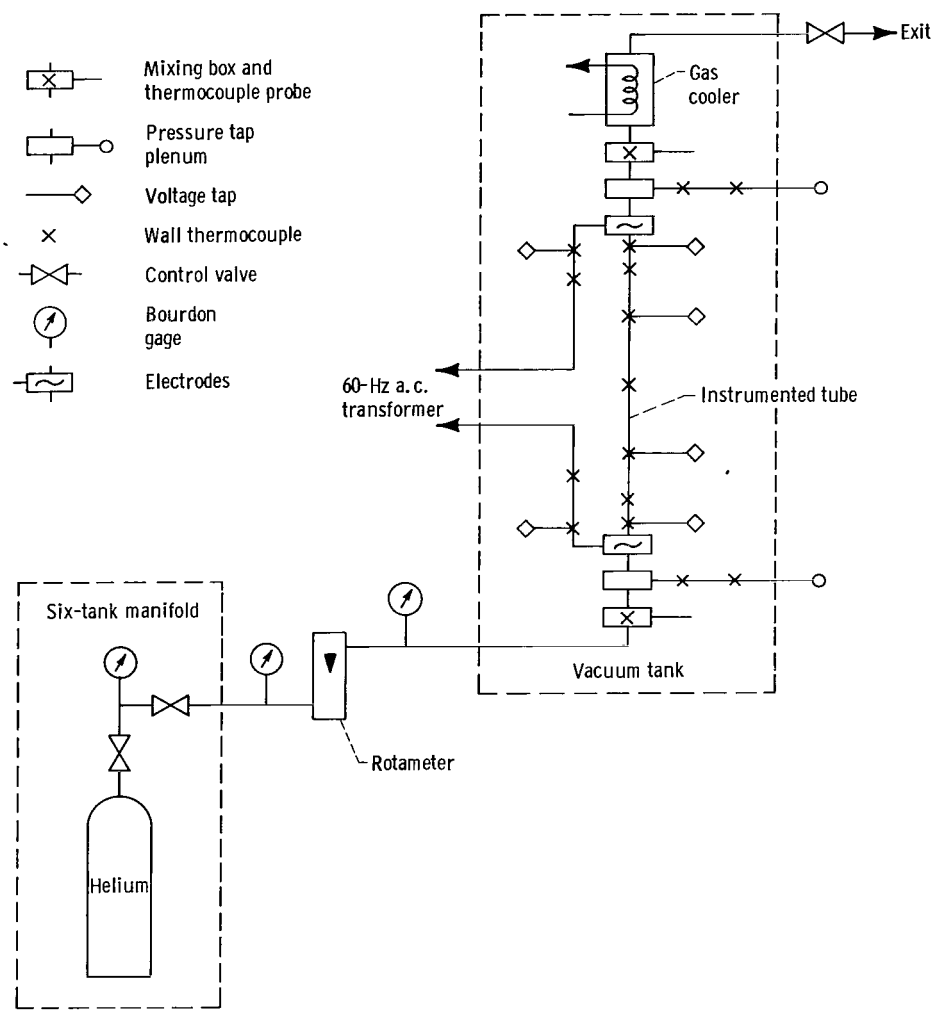

Figure 2. - Flow schematic of heat-transfer test stand.

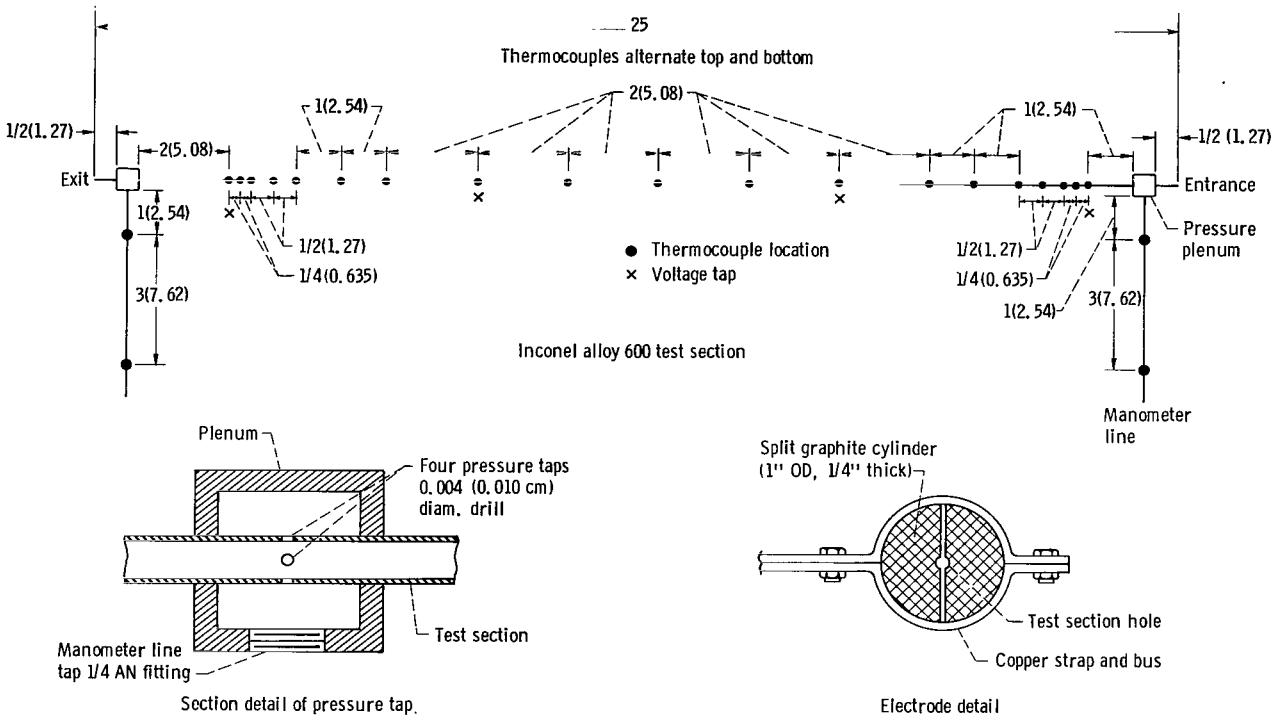

Figure 3. - Test stand instrumentation. (All dimensions are in inches (cm).)

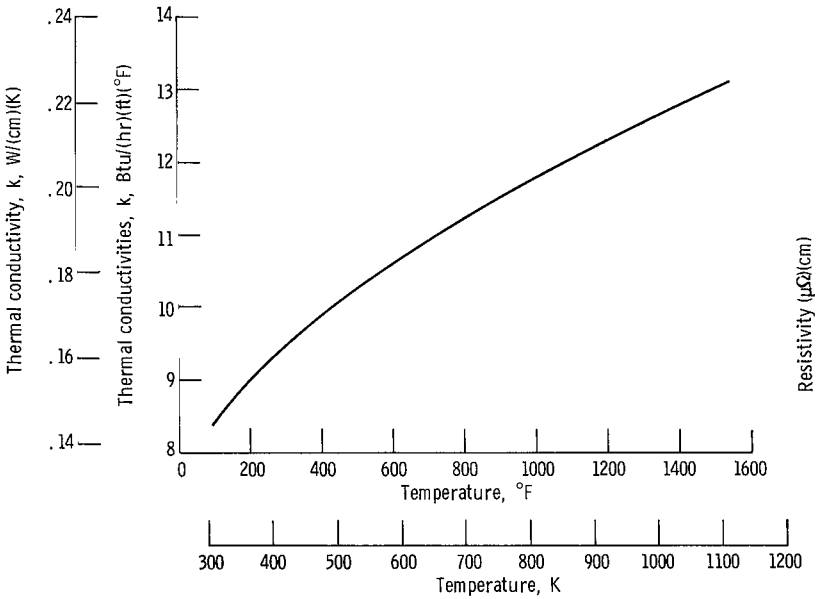

(a) Thermal conductivity (ref. 12).

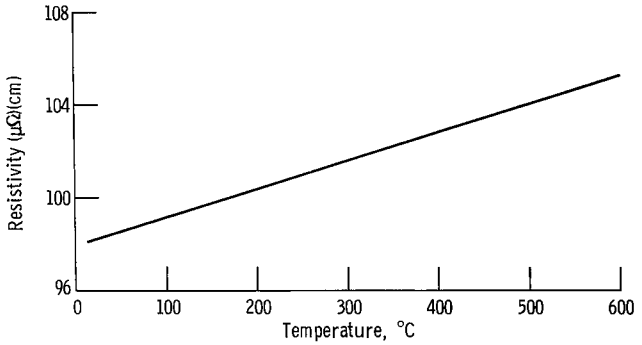

(b) Resistivity (ref. 11, pg. 1123).

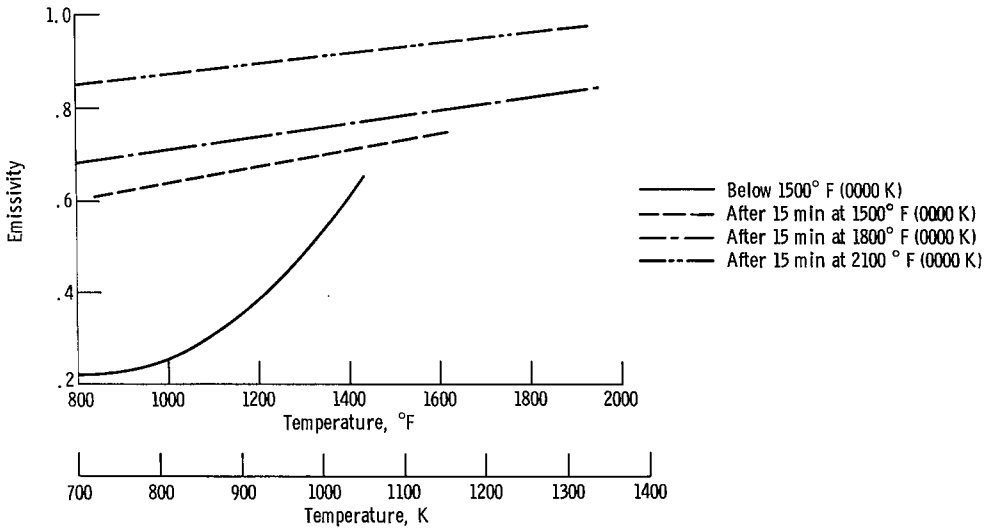

(c) Total emissivity of sheet as rolled (ref. 12).

Figure 4. - Thermal properties of Inconel alloy 600.

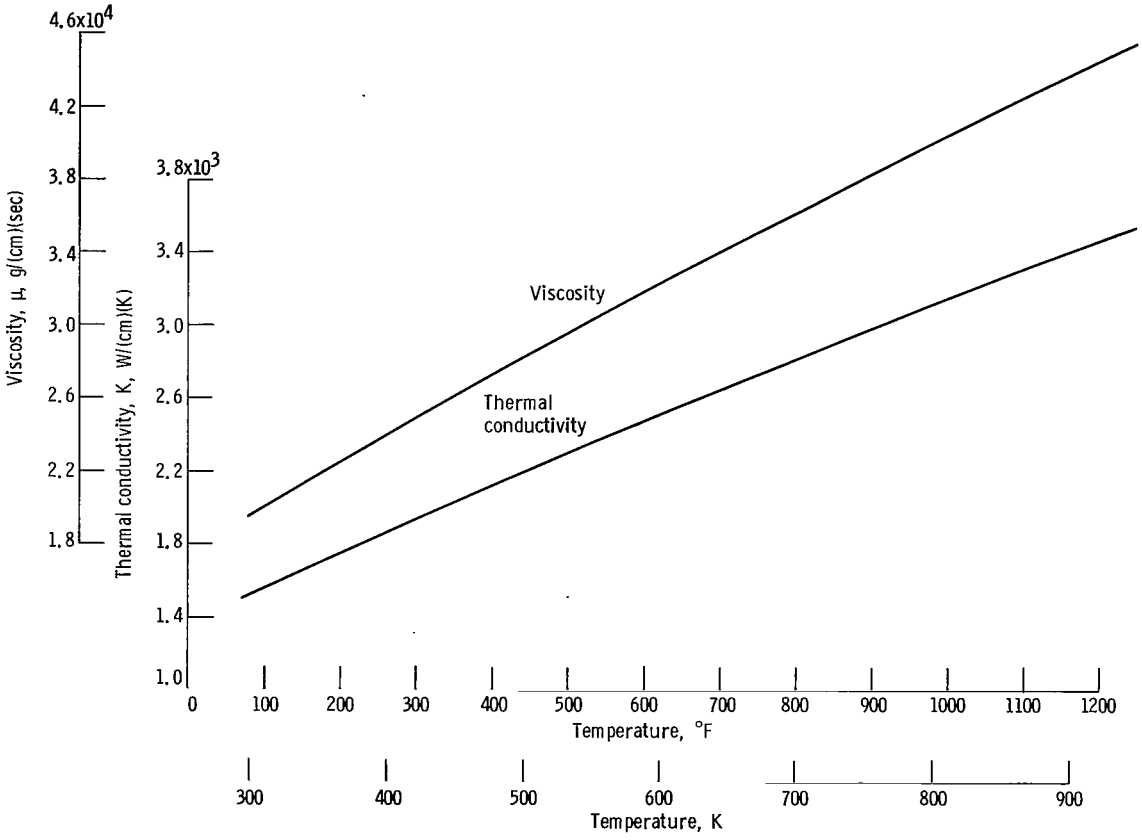

Figure 5. - Helium gas properties (ref. 16).

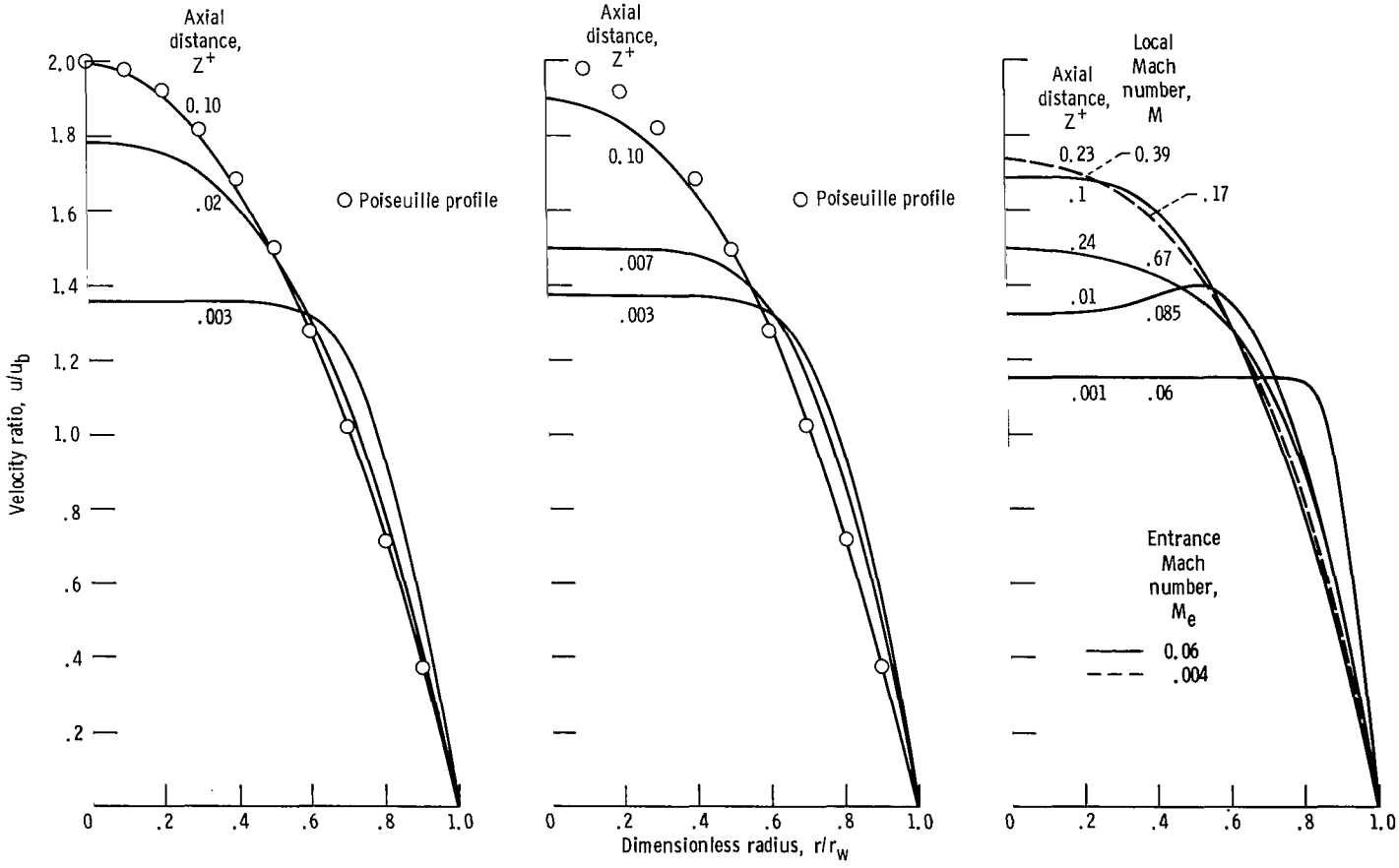

(a) Wall heat flux, 0.135; entrance Mach number, 0.06.

(b) Wall heat flux, 1.35; entrance Mach number, 0.06.

(c) Wall heat flux, 13.5.

Figure 6. - Development of radial velocity profiles.

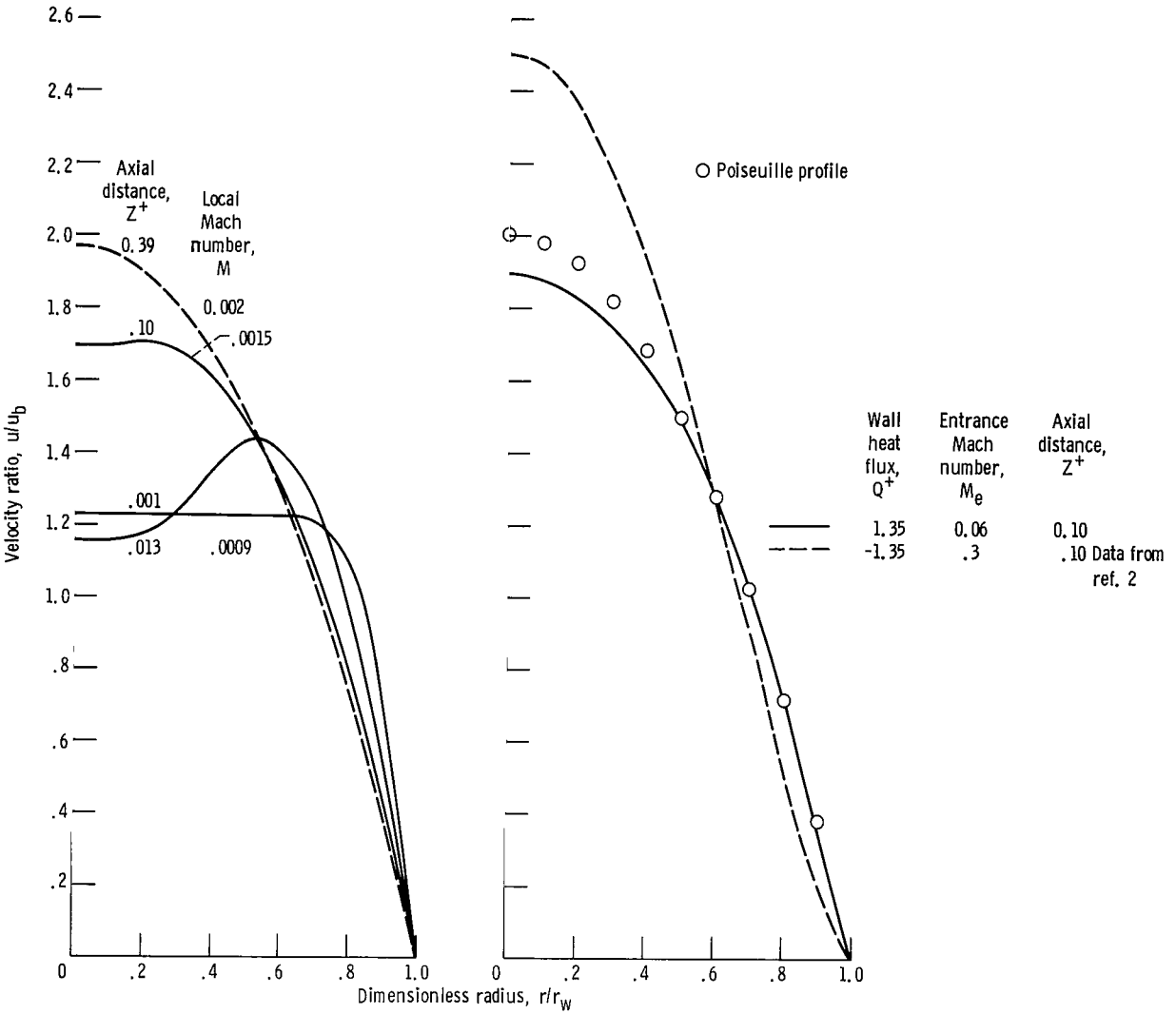

(d) Wall heat flux, 27.0; entrance Mach number, 0.0005.

(e) Wall heat flux, 1.35; comparison with cooling case.

Figure 6. - Concluded.

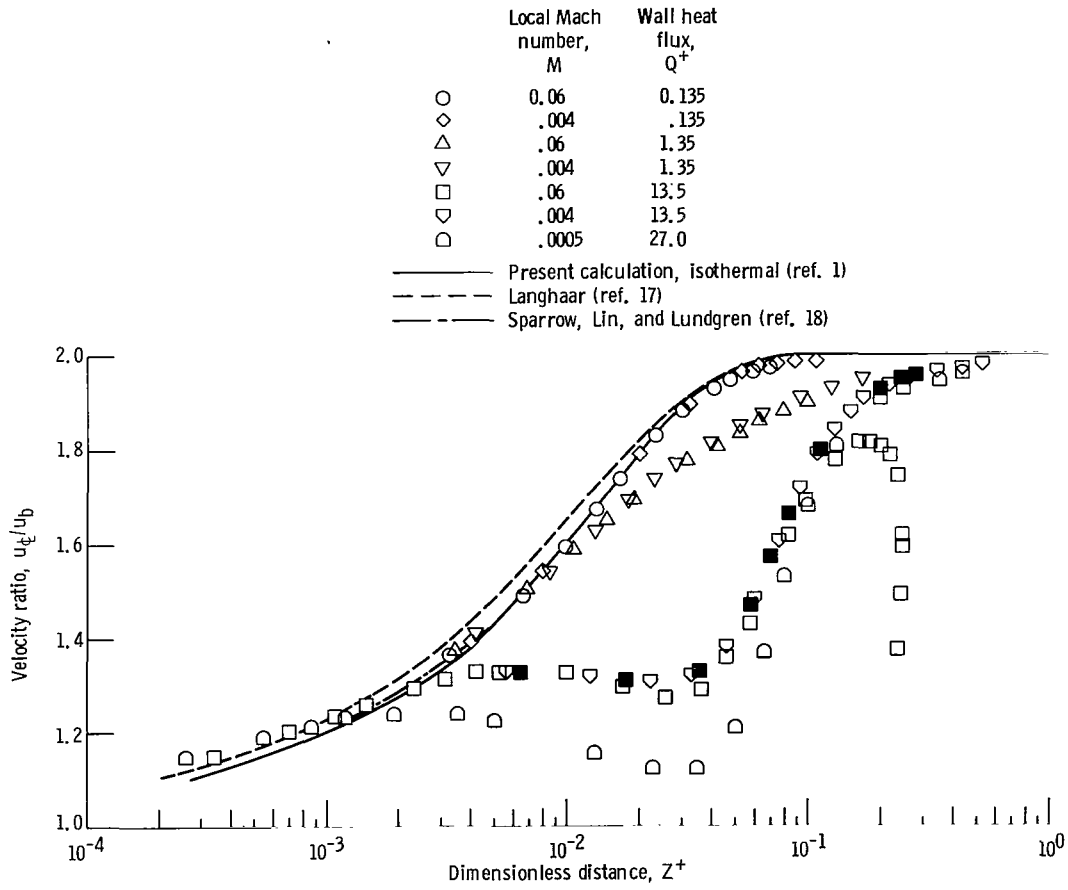

Figure 7. - Axial development of centerline velocity ratio.

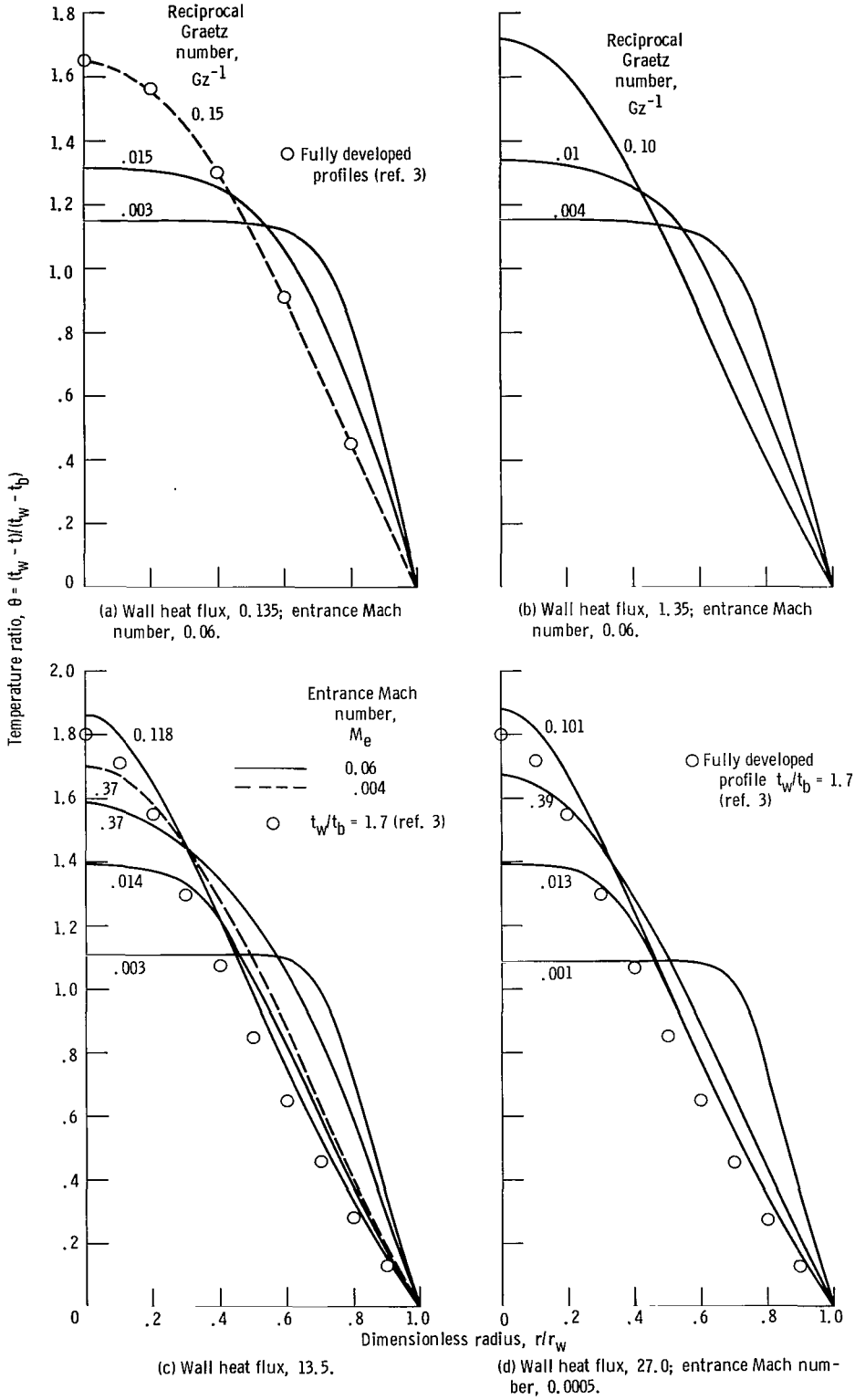

Figure 8. - Development of temperature profiles.

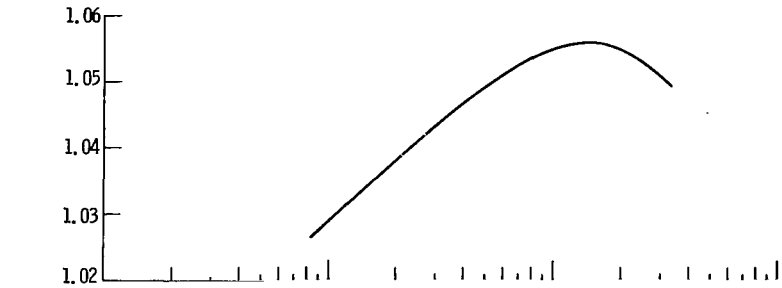

(a) Wall heat flux, 0.135; entrance Mach number, 0.06.

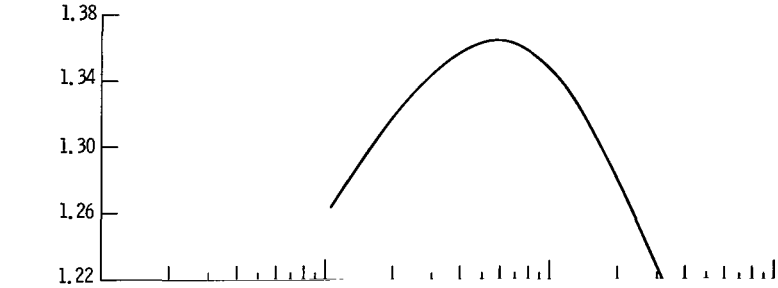

(b) Wall heat flux, 1.35; entrance Mach number, 0.06.

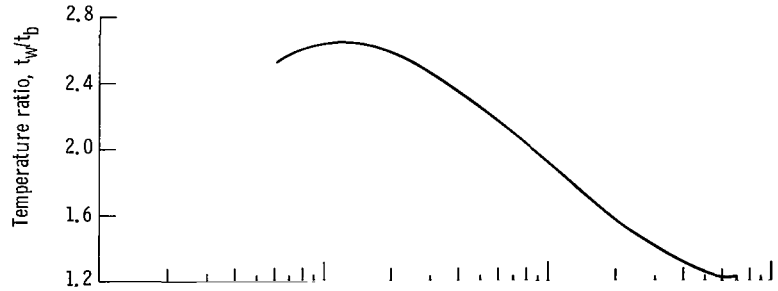

(c) Wall heat flux, 13.5; entrance Mach number, 0.06.

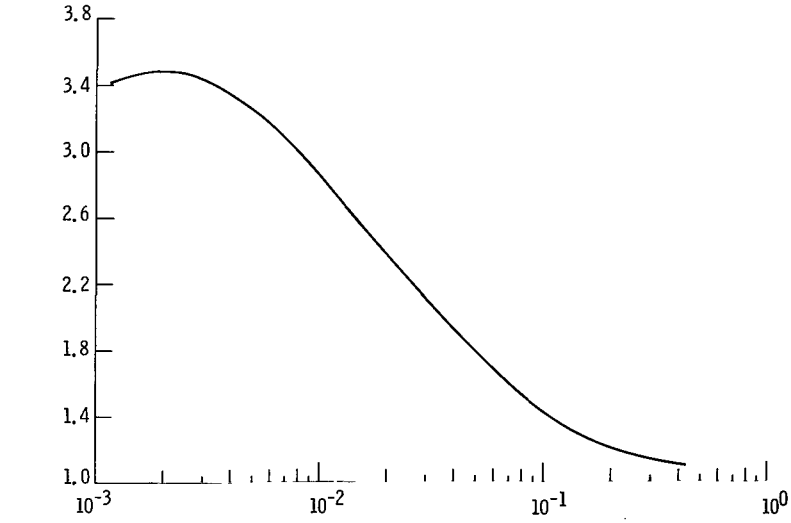

(d) Wall heat flux, 27.0; entrance Mach number, 0.0005.

Figure 9. - Variation of wall- to bulk-temperature ratio along tube axis.

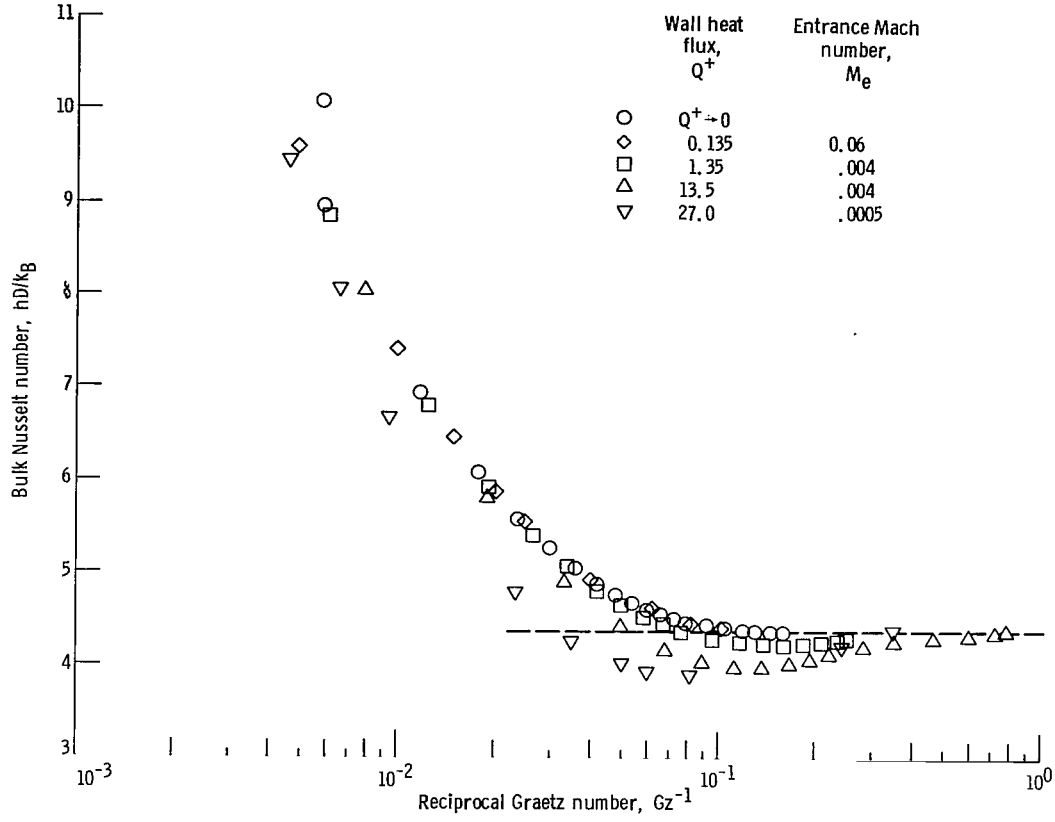

Figure 10. - Numerical results for Nusselt number development with several heat fluxes.

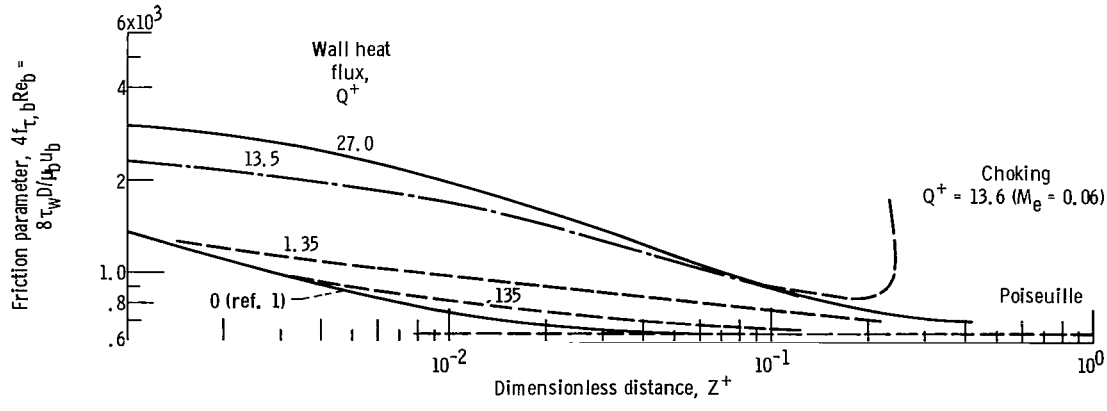

Figure 11. - Numerical results for local laminar friction parameter based on wall shear.

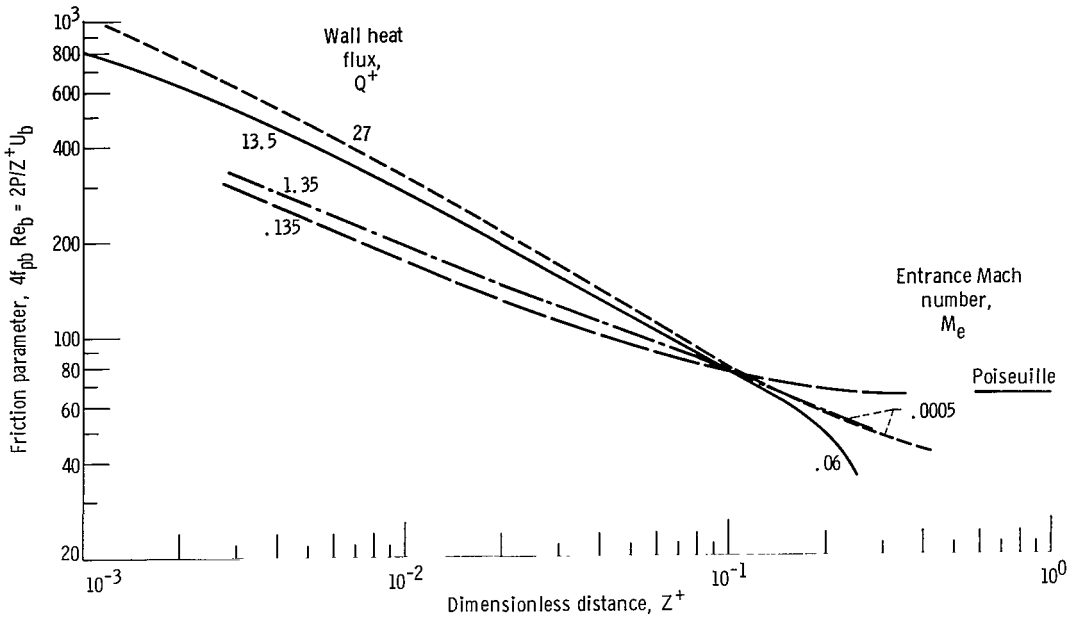

Figure 12. - Numerical results for friction parameter based on pressure drop.

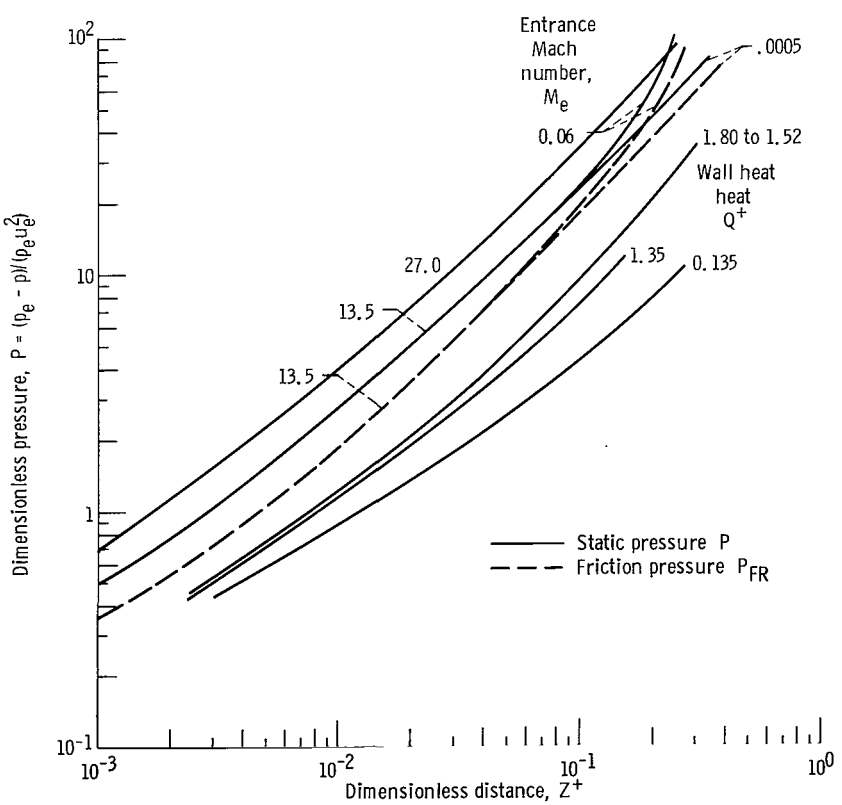

Figure 13. - Dimensionless pressure development along tube length.

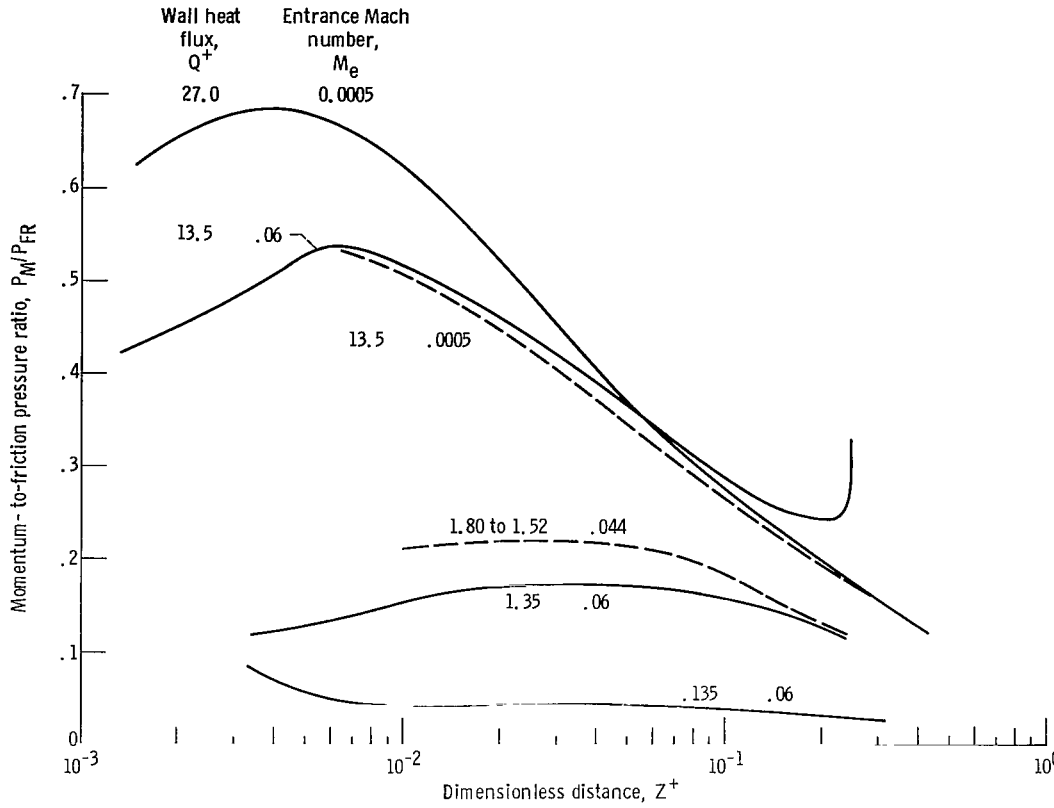

Figure 14. - Development of ratio of momentum pressure to friction pressure along tube length.

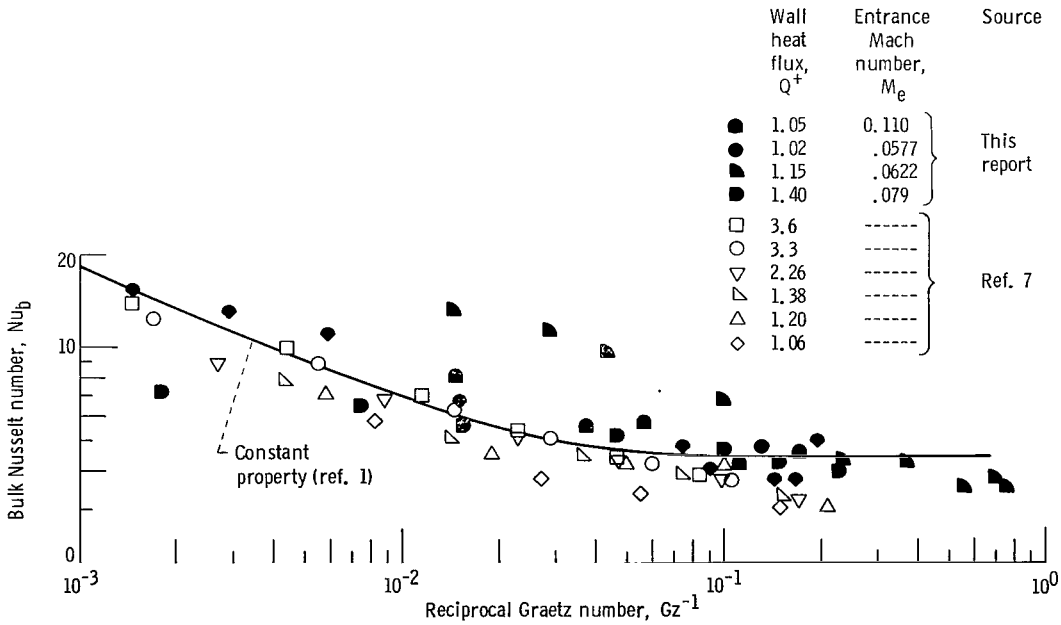

Figure 15. - Comparison of experimental heat-transfer data for uniform heat flux.

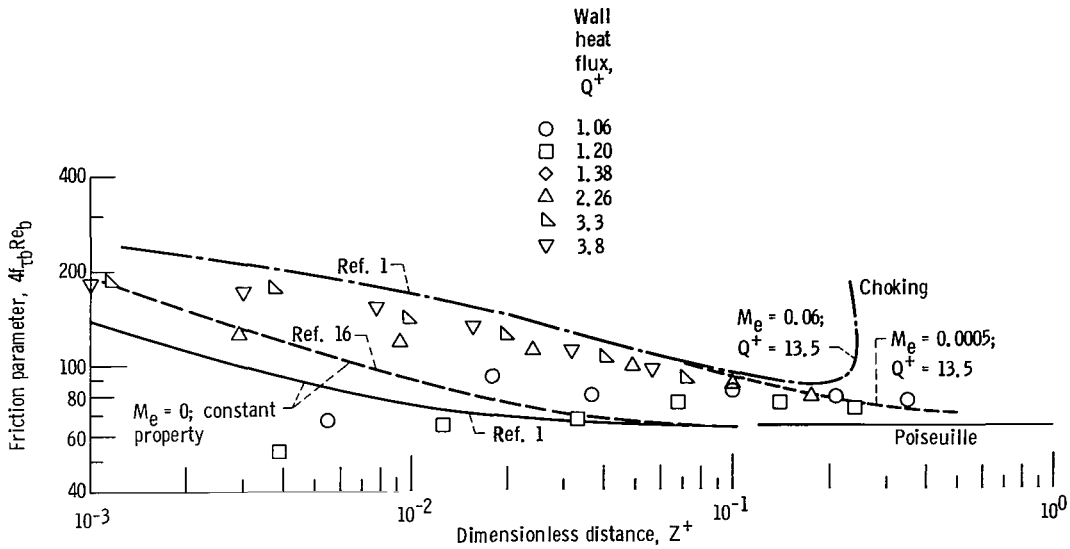

Figure 16. - Comparison of experimental friction factors of reference 7 with numerical results (helium data).

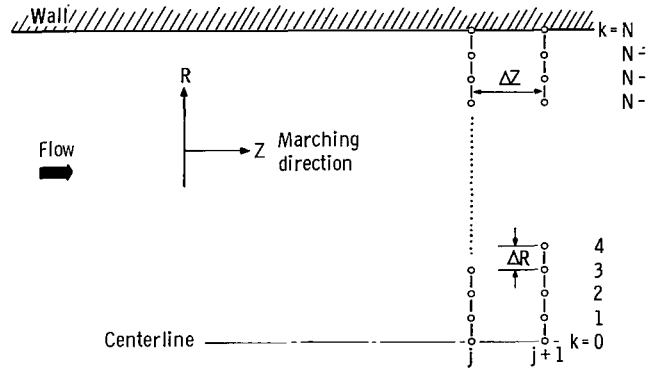

Figure 17. - Finite difference mesh for numerical solution of the boundary-layer equations.

"The aeronautical and space activities of the United States shall be conducted so as to contribute . . . to the expansion of human knowledge of phenomena in the atmosphere and space. The Administration shall provide for the widest practicable and appropriate dissemination of information concerning its activities and the results thereof."

—NATIONAL AERONAUTICS AND SPACE ACT OF 1958

NASA SCIENTIFIC AND TECHNICAL PUBLICATIONS

TECHNICAL REPORTS: Scientific and technical information considered important, complete, and a lasting contribution to existing knowledge.

TECHNICAL NOTES: Information less broad in scope but nevertheless of importance as a contribution to existing knowledge.

TECHNICAL MEMORANDUMS: Information receiving limited distribution because of preliminary data, security classification, or other reasons.

CONTRACTOR REPORTS: Scientific and technical information generated under a NASA contract or grant and considered an important contribution to existing knowledge.

TECHNICAL TRANSLATIONS: Information published in a foreign language considered to merit NASA distribution in English.

SPECIAL PUBLICATIONS: Information derived from or of value to NASA activities. Publications include conference proceedings, monographs, data compilations, handbooks, sourcebooks, and special bibliographies.

TECHNOLOGY UTILIZATION PUBLICATIONS: Information on technology used by NASA that may be of particular interest in commercial and other non-aerospace applications. Publications include Tech Briefs, Technology Utilization Reports and Technology Surveys.

Details on the availability of these publications may be obtained from:

SCIENTIFIC AND TECHNICAL INFORMATION OFFICE

NATIONAL AERONAUTICS AND SPACE ADMINISTRATION

Washington, D.C. 20546